Title: Serum amyloid A3 deficiency modulates aortic immune composition and attenuates murine atherosclerosis progression

Authors: Tzu-Yin Chou[1,2], Yu-Zhen Ye[1,2], Chia-Jung Lien[1], Jui-Chun Wang[1], Chen-Hsuan Yang[1], Yen-Ting Chen[1], Pei-An Chao[1], Jian-Da Lin[1]*

Affiliations:

[1]Department of Biochemical Science and Technology, National Taiwan University, Taipei 10617, Taiwan

[2]These authors contributed equally.

* Correspondence to:

jdlin@ntu.edu.tw

Abstract

Atherosclerosis is a growing concern in developed nations, necessitating the identification of therapeutic targets for advancing personalized medicine. Serum amyloid A3 (*Saa3*) has been linked to accelerated plaque progression by affecting cholesterol metabolism and modulation of inflammation. We hypothesize that knocking out *Saa3* (*Saa3*$^{-/-}$) could mitigate plaque development by regulating aortic immune cell compositions during atherosclerosis progression. Using a murine model, we induced atherosclerosis via a gain-of-function mutant PCSK9-encoding adeno-associated viral vector (AAVmPCSK9) in female wild-type (WT) and *Saa3*$^{-/-}$ mice. *Saa3*$^{-/-}$ mice developed smaller plaques than WT mice, and single-cell RNA sequencing revealed significant differences in aortic immune cell populations, particularly among aortic macrophages. Aortic macrophages in atherosclerotic *Saa3*$^{-/-}$ mice represent an anti-inflammatory and tissue-repairing phenotype and the Trem2^{hi} macrophages, characterized by high *Gpnmb*, *Lpl*, and *Spp1* expressions, predominated over the typical foamy macrophages in *Saa3*$^{-/-}$ compared to WT mice. Notably, SAA3 regulates cholesterol metabolism and inflammatory responses in foamy macrophages. Our study highlights *Saa3* as a key modulator of aortic immune cells that impact atherosclerosis progression.

35 ## Introduction

36 Atherosclerosis, a major cardiovascular concern in developed countries [1], is a
37 chronic arterial disease characterized by plaque formation within arterial walls. This
38 process involves complex interplays among various cellular components and
39 inflammatory mediators that drive inflammation and lipid accumulation.
40 Atherosclerosis initiation involves low-density lipoprotein (LDL) accumulation in the
41 coronary artery intima, which upon oxidation to ox-LDL by risk factors, activates
42 nuclear factor kappa B (NF-κB) [2, 3]. This leads to the expression of adhesion
43 molecules like vascular cell adhesion molecule-1 (VCAM-1) and intercellular adhesion
44 molecule-1 (ICAM-1) on the endothelium, aiding monocyte recruitment into the
45 vascular wall [4]. These recruited monocytes then convert into macrophages under the
46 influence of macrophage colony-stimulating factor (M-CSF), and release inflammatory
47 cytokines such as interleukin (IL)-1β, IL-12, and tumor necrosis factor (TNF)-α,
48 escalating the inflammatory response [5]. As the disease progresses, these macrophages
49 become foam cells by uptaking ox-LDL, which is crucial for plaque formation and
50 intimal thickening.

51 Macrophages are the predominant type of immune cell found in aortic plaques but
52 display a wide range of phenotypes and functions. At the onset of atherosclerosis,

53 macrophages ingest ox-LDL via receptors like CD36 and SR-A, forming cholesterol-
54 rich foam cells. Continued lipid intake without effective cholesterol removal leads to
55 foam cell death, creating a necrotic core in advanced plaques [6, 7]. Single-cell RNA
56 sequencing (scRNA-seq) of monocyte-derived macrophages has revealed that
57 macrophage heterogeneity is beyond M1/M2 definitions and associated with different
58 states of atherosclerosis, where progression is linked to more complex states than
59 regression [8]. This technique has revealed various macrophage subsets within
60 atherosclerotic plaques, each characterized by unique markers and roles contributing
61 to aortic plaque progression or regression. Notably, three main groups are identified:
62 tissue-resident-like macrophages, marked by *Folr2* and *Lyve1*, which promote tissue
63 stability; inflammatory macrophages, with markers such as *Tnf* and *Il1b*, which
64 activate immune responses; and anti-inflammatory TREM2^{hi} macrophages, associated
65 with cholesterol metabolism and identified by markers such as *Trem2* [9, 10]. This
66 diversity in macrophage functions underscores the complexity of atherosclerosis and
67 offers multiple targets for therapy.
68 The Serum Amyloid A (SAA) protein family, including SAA3, represents a group of
69 acute-phase proteins central to immune responses and inflammatory processes. Unlike
70 humans, who lack a functional SAA3 protein due to a premature stop codon and
71 resulting frameshift mutation that renders the SAA3 gene a pseudogene [11], mice

72 express a functional SAA3 and mouse SAA3 shares 70% amino acid homology with
73 human SAA1 [12]. Its tissue distribution and expression patterns, particularly in
74 adipose tissue, align more closely with human SAA1 than with mouse SAA1 or
75 SAA2, suggesting a functional similarity between mouse SAA3 and human SAA1
76 [12]. Furthermore, sex-dimorphisms have been reported in the context of
77 atherosclerosis, SAA3-associated inflammatory responses, and microbiota-mediated
78 regulation of immune and metabolic processes. Smit et al. (2024) found that in aged
79 atherosclerotic *Ldlr*$^{-/-}$ mice, plaque volume was similar between males and females,
80 but female mice presented plaques with higher collagen and cholesterol crystal
81 content, along with a smaller necrotic core and fewer macrophages compared to males
82 [13]. *Saa3* has been shown to have sexually dimorphic effects on atherosclerosis, with
83 deficiency being atheroprotective in male mice but being proatherogenic in female
84 mice [14]. This response is suggested to be influenced by sex steroids, as 17β-
85 estradiol promotes a pro-inflammatory profile in male *Saa3*$^{-/-}$ macrophages [14].
86 However, another study indicates a significant upregulation of SAA3, but not SAA1
87 or SAA2, in the adipose tissue of conventional mice, compared to germ-free mice
88 [15]. The presence of intestinal microbiota significantly upregulated SAA3 expression
89 in adipose tissue and colonic tissue, with evidence indicating that its colonic
90 regulation is partially mediated through the Toll-like receptor (TLR)/MyD88/NF-κB

91 signaling axis [12]. These data suggest that *Saa3*-associated sex-specific differences
92 in atherosclerosis progression and inflammatory responses may result from its
93 interaction with confounding factors, such as the microbiota, which modulate SAA3
94 levels and sex dimorphism in atherosclerosis.

95 Previous studies suggest that mouse *Saa3* modulates local injury and inflammatory
96 responses, as its mRNA and protein expression in macrophages increases with the
97 dose of lipopolysaccharide (LPS) [12]. It also indicates that increased SAA expression
98 correlates with the aortic plaque progression in $ApoE^{-/-}$ mice, accompanied by
99 elevated levels of IL-6 and TNF-α. This upregulation potentially facilitates the
100 infiltration of M1 macrophages into atherosclerotic regions, thereby promoting
101 atherosclerosis progression [16]. Mouse *Saa3* is actively expressed, predominantly in
102 macrophages and adipose tissues [17], and the activation of the *Saa3* promoter is
103 regulated through C/EBPβ signaling, which in turn activates macrophages,
104 underscoring the complex interaction within adipose tissue [18]. Pulmonary exposure
105 to nanoparticles induces pronounced acute phase responses, with mouse *Saa3*
106 identified as the most differentially regulated gene, demonstrating prolonged
107 upregulation in lung tissue and correlating with neutrophil infiltration and systemic
108 SAA3 protein levels [19]. Notably, SAA3 has been reported to promote
109 atherosclerosis, and overexpressed SAA3 increases atherosclerotic plaque size [20].

110 Overall, these studies support the role of SAA3 in regulating macrophage function
111 during atherosclerosis, though the specific type of aortic macrophages that regulate
112 aortic plaque progression and the underlying mechanisms remain elusive.
113 To assess how *Saa3* deficiency impacts aortic immune cell composition and
114 functionalities in contributing to atherosclerosis progression, we applied scRNA-seq
115 using the BD Rhapsody platform on immune cells from aortic arches of female *Saa3*
116 knockout (*Saa3*$^{-/-}$) mice and littermate wild-type (WT) control mice during
117 atherosclerosis. Our investigation seeks to delineate the impact of *Saa3* deficiency on
118 the phenotypic and functional landscape of aortic macrophages and other immune cell
119 populations. By comparing the immune cell profiles between *Saa3*$^{-/-}$ and WT mice,
120 we aim to uncover the molecular mechanisms by which SAA3 influences macrophage
121 or other immune cell types-mediated aortic plaque progression.
122

123 Results

124 *Saa3* deletion reduced aortic plaque progression but increased peripheral lipid
125 levels

126 To determine the phenotype of atherogenesis after *Saa3* deficiency, we utilized a
127 C57BL/6 wild-type (WT) mouse-based atherosclerosis model independent of *Ldlr*$^{-/-}$
128 mice breeding [8, 21, 22]. Plaque progression was initiated by injecting the mice with

129 an adeno-associated viral vector expressing a gain-of-function mutant of protein
130 convertase subtilisin/kexin type 9 (AAVmPCSK9), resulting in LDL receptor
131 deficiency and hypercholesterolemia. Both female C57BL/6 WT and C57BL/6 *Saa3*$^{-/-}$
132 mice were treated with AAVmPCSK9 and fed the Western diet (WD) for 18 weeks to
133 induce hypercholesterolemia and aortic plaque formation. We longitudinally collected
134 plasma from mice at 0, 2, 4, 8, 12, and 16 weeks on WD, and the immune profiling
135 was performed on sorted CD45+ cells from aortic arches by single-cell RNA-seq at
136 18 weeks on WD (Fig. 1a). We first determined total cholesterol levels in the plasma
137 of WT and *Saa3*$^{-/-}$ mice and a baseline comparison at weeks 0 revealed no significant
138 differences, with levels below 100 mg/dL (Fig. 1b). Over time, *Saa3*$^{-/-}$ mice
139 developed higher cholesterol levels than WT, with a slight increase at weeks 2
140 through 12, and a significant rise by weeks 16 (Fig. 1b).
141 Research demonstrates that serum amyloid A (SAA) attenuates the anti-
142 inflammatory and antioxidative functions of high-density lipoprotein (HDL) by
143 facilitating its binding to adipocyte and macrophage-derived glycoproteins [23]. We
144 conducted high-density lipoprotein (HDL)/ low-density lipoprotein LDL analyses that
145 revealed an increase in peripheral HDL levels during the initial phase of
146 atherosclerosis progression (Fig. 1c). Not only did HDL levels demonstrate a rising
147 trend with statistically significant increases in the *Saa3*$^{-/-}$ group compared to WT at
148 weeks 2 and 4, but the absence of *Saa3* also correlated with a potential increase in
149 LDL levels in the bloodstream (Fig. 1c).
150 Overexpression or suppression of SAA3 can increase or decrease aortic lesion area
151 in *ApoE*$^{-/-}$ mice [20]. We also determined aortic plaque sizes between WT and *Saa3*$^{-/-}$
152 mice by histologically evaluating aortic root sections stained with Oil Red O (Fig.
153 1d). It demonstrated a significant decrease in plaque area in *Saa3*$^{-/-}$ compared to WT

154 mice, with mean values of 31.50% and 45.48%, respectively (Fig. 1e). These
155 observations demonstrate that *Saa3* deficiency increases peripheral lipid levels but
156 attenuates aortic plaque formation, suggesting the complex roles of *Saa3* in
157 modulating lipid metabolism and atherogenesis.
158

159 **_Saa3_ deficiency alters intercellular immune communications in aortic arches**
160 **during atherosclerosis progression**

161 All immune cells express CD45, a major transmembrane glycoprotein expressed on
162 all hematopoietic cells [24] and some cardiac fibroblasts [25]. To elucidate the
163 immunological impact of *Saa3* deficiency within the aortic arch and its putative role
164 in the pathogenesis of atherosclerosis, we performed a single-cell RNA sequencing on
165 FACS-purified CD45+ cells (Supplementary Fig. 1). After data processing, possible
166 contaminated cell removement, anchor-based dataset integration [26], and cell
167 clusters visualized by Uniform Manifold Approximation and Projection (UMAP), it
168 revealed the immune cell compositional variances in aortic arches between female
169 WT and *Saa3*$^{-/-}$mice during atherosclerosis progression (Fig. 2). Utilizing the cell
170 annotation tool by *SingleR* [27], we classified the cell phenotypes, enabling initial
171 taxonomical segregation within the distinct clusters (Fig. 2a). Our analysis identified
172 9 cell subpopulations, encompassing B cells, dendritic cells (DCs), innate lymphoid
173 cells (ILCs), macrophages, monocytes, neutrophils, natural killer T (NKT) cells, T
174 cells, and γδ T cells (Tgd) (Fig. 2a). Despite similar UMAP topologies between WT
175 and *Saa3*$^{-/-}$ aortic cell populations (Fig. 2a), *Saa3*$^{-/-}$ mice showed increased T cells, B
176 cells, monocytes, γδ T cell, and neutrophils proportions but decreased macrophages,
177 innate lymphoid cells (ILC), and NKT cells compared to WT mice (Fig. 2b).

178 Heatmaps of differential gene expression profiles supported these *SingleR*-annotated
179 cell type differences, highlighting the top 5 marker genes per subset (Fig. 2c).
180 *Cellchat* has been used to infer, analyze, and visualize cell-cell communication
181 networks in scRNA-seq datasets [27]. To dissect the variances in signaling dynamics
182 in aortic cell types between WT and *Saa3*$^{-/-}$ mice, we employed *CellChat* to evaluate
183 the intercellular communication networks and assess the number and intensity of
184 cellular interactions within the respective cohorts (Figs. 2d-2e). The resultant metrics
185 demonstrated 1,822 and 1,787 interactions across all cell types in aortic arches
186 between WT and *Saa3*$^{-/-}$ mice, with interaction strength for *Saa3*$^{-/-}$ cell types
187 quantified at 83.957 compared to 64.762 for WT (Fig. 2d). To rigorously dissect the
188 discrete intercellular communication patterns responsible for the observed differential
189 signaling, we interrogate the heatmaps that delineate both the frequency and
190 magnitude of interaction strengths across aortic cell types (Fig. 2e). Increased
191 magnitude of intercellular interaction strengths was observed in the aortic arches of
192 *Saa3*$^{-/-}$ mice compared to their WT mice (Fig. 2d). The increased interaction
193 magnitudes were primarily directed from most immune cells toward γδ T cells (Tgd),
194 while reduced interactions were directed from macrophages toward other immune
195 cells in *Saa3*$^{-/-}$ mice compared to WT mice (Fig. 2e). These patterns suggest that the
196 absence of the *Saa3* gene exerts a profound regulatory influence on the intercellular
197 communication network among immune cells, potentially revealing critical insights
198 into the regulatory mechanisms of immune function within the aortic niche.
199

200 ***Saa3* depletion increases biological processes in aortic macrophages that are**
201 **highly associated with lipid metabolism and inflammatory recruitment during**

202 **atherosclerosis**

203 *CellChat* analysis revealed significant differences in cell-cell interaction signals
204 between aortic macrophages and other aortic immune cell populations within the
205 *Saa3*$^{-/-}$ and WT group (Figs. 2d-2e). To delve deeper, we assessed the transcriptomic
206 variances in macrophages from *Saa3*$^{-/-}$ versus WT mice. Our volcano plot delineated
207 distinct gene expression profiles, with genes such as *Fabp5* and *Gpnmb* are
208 upregulated in *Saa3*$^{-/-}$ mice, exceeding the established $\log_2$ fold change threshold of
209 >1 and p-values < 0.01 (Fig. 2f). *Fabp5*, which plays a central role in the intracellular
210 transport of lipids, is integral to the uptake, transport, and metabolism of fatty acids
211 [28]. *Gpnmb* has been shown to protect against obesity-related metabolic disorders by
212 mitigating macrophage inflammatory capacity [29]. Conversely, genes such as
213 *Cxcl13*, *Lyz1*, *Tmem176a*, *Clec4a1*, *C3*, and *Cfp* are downregulated in *Saa3*$^{-/-}$
214 macrophages (Fig. 2f). Studies have demonstrated that a lack of *Cxcl13* correlates
215 with a diminished presence of atherosclerotic conditions, likely due to lower
216 recruiting inflammatory granulocytes within the lesions [30] [31]. *C3* expression in
217 macrophages has been linked to exacerbating atherosclerosis by limiting macrophage
218 efferocytosis, contributing to plaque development and inflammation [32]. *Cfp* has
219 been linked to regulating complement activation and orchestrating iron homeostasis
220 [33]. Gene set enrichment analysis, conducted using the *ClusterProfiler* package [34],
221 revealed distinct gene ontology (GO) pathways in aortic macrophages (Fig. 2g). WT
222 aortic macrophages were enriched for pathways associated with enhanced immune
223 cell recruitment and chemotaxis, whereas *Saa3*$^{-/-}$ aortic macrophages exhibited
224 enrichment for pathways related to lipid localization and transport (Fig. 2g,
225 Supplementary Table 1). Overall, these data suggest the phenotypes of aortic
226 macrophages were impacted by reduced recruitment of inflammatory macrophages,

227 which helped mitigate inflammation potentially influencing lesion formation and
228 stability.
229

230 **Altered macrophage compositions and enhanced Trem2^{hi} macrophage presence**
231 **linked to diminished aortic plaque progression in *Saa3*$^{-/-}$ mice**

232 Macrophage (Mφ) polarization, along with several distinct clusters, has been
233 identified as increasingly prevalent during the atherosclerosis progression than
234 regression [8, 35]. To dissect the functional heterogeneity of aortic macrophage
235 populations in WT and *Saa3*$^{-/-}$ mice during atherosclerosis, we classified macrophages
236 into subpopulations and compared the top differentially expressed genes from each
237 cluster against our previously published dataset, where we profiled single-cell sorted
238 *Cx3cr1*-derived aortic macrophages from lineage-tracing mice during atherosclerosis
239 progression and regression (hereinafter referred to as "*Lin regression study*")[8].
240 There are five distinct macrophage clusters in the aortic arches of WT and *Saa3*$^{-/-}$
241 mice during atherosclerosis (Fig. 3a). CD74^{hi}MHCII^{hi} Mφ is the most abundant
242 macrophage subset in both genotypes, with CD74^{hi}MHCII^{hi}, Folr2^{hi}, and
243 Retnla^{hi}Ear2^{hi} Mφ being more prevalent in WT mice compared to *Saa3*$^{-/-}$ mice (Fig.
244 3b). Conversely, Trem2^{hi} and Apbb2^{hi} Mφ are found in higher percentages within the
245 aortic arches of *Saa3*$^{-/-}$ mice than WT mice (Fig. 3b).
246 The Cd74^{hi}MHCII^{hi} Mφ, a subset identified through the *Lin regression study* [8], is
247 characterized by high expression of genes such as *Tmem176b*, *Lilra5*, *H2-Eb1*, and
248 *H2-Aa* (Supplementary Fig. 2a and Table 2). Folr2^{hi} Mφ exhibit unique transcriptional
249 profiles with *F13a1, Pf4, Folr2*, and *Lyve1* (Supplementary Fig. 2a and Table 2).
250 These markers are indicative of a tissue-resident-like macrophage phenotype [36-39]

251 and align with the molecular signature of the Folr2^{hi} macrophage cluster previously
252 delineated in the *Lin regression study* [8]. Retnla^{hi}Ear2^{hi} Mφ is distinguished by their
253 elevated expression of genes such as *Retnla* and *Ear2*, which suggest an early-stage
254 transition of monocytes to macrophages within tissues [40, 41]. Additionally, these
255 macrophages show enrichment in genes like *Gm2a* and *Fn1*, confirming their
256 specialized state as identified in the *Lin regression study* [8]. Trem2^{hi} Mφ is defined
257 by a gene expression signature that mirrors the population described by *Cochain et al.*
258 [42] and *Lin regression* [8] studies and is exemplified by heightened expression of
259 *Ctsd, Lgals3, Spp1*, and *Lpl* (Supplementary Fig. 2a and Table 2). Apbb2^{hi} Mφ is
260 characterized by the predominant expression of *Cd9, Cd72*, and *Hexb* genes. While
261 sharing traits with the "Trem2^{hi} Mφ," they are uniquely distinguished by their
262 expression of *Apbb2* (Supplementary Fig. 2a and Table 2).
263 On the other hand, we identified differentially expressed genes (DEGs) across five
264 macrophage populations and conducted gene ontology (GO) enrichment analysis on
265 biological pathways to explore potential functions (Supplementary Fig. 2b and Table
266 3). Compared to other macrophage clusters, Cd74^{hi}MHCII^{hi} Mφ in the aortic arches
267 showed significant enrichment in pathways related to leukocyte-mediated immunity,
268 positive regulation of cell activation, activation of the immune response, and
269 immunoglobulin-mediated immune responses (Supplementary Fig. 2b and Table 3).
270 Folr2^{hi} Mφ is distinguished by activation of immune response, ameboidal-type cell
271 migration, cell chemotaxis, regulation of angiogenesis, and regulation of viral
272 processes (Supplementary Fig. 2b and Table 3). Retnla^{hi}Ear2^{hi} Mφ were noted for
273 their leukocyte proliferation, mononuclear cell proliferation, positive regulation of
274 leukocyte cell-cell adhesion, positive regulation of T cell activation, and response to
275 type II interferon (Supplementary Fig. 2b and Table 3). Trem2^{hi} Mφ is characterized

276 by the generation of precursor metabolites and energy, aerobic respiration, oxidative
277 phosphorylation, purine ribonucleoside triphosphate biosynthetic process, and ATP
278 biosynthetic process (Supplementary Fig. 2b and Table 3). These functions highlight
279 the metabolic specialization of Trem2^{hi} Mφ in energy production and biosynthesis.
280 Apbb2^{hi} Mφ demonstrated upregulation in myeloid cell differentiation, leukocyte
281 migration, actin filament organization, regulation of protein-containing complex
282 assembly, and mononuclear cell migration (Supplementary Fig. 2b and Table 3).
283 In *Lin regression study* [8], Cd74^{hi}MHCII^{hi} Mφ and Retnla^{hi}Ear2^{hi} Mφ are abundant
284 in aortic arches of progression group and we also observed these two subsets are
285 higher in aortic arches of WT mice compared to *Saa3*$^{-/-}$ mice (Fig. 3b). *Folr2*
286 expression is increased in human atherosclerotic plaques compared to normal arterial
287 tissue[43] and we also observed aortic Folr2^{hi} Mφ are higher in WT mice than *Saa3*$^{-/-}$
288 mice (Fig. 3b). Trem2^{hi} Mφ exhibits comparable prevalence between the progression
289 and regression cohorts in the *Lin regression study* [8], whereas both Trem2^{hi} and
290 Apbb2^{hi} Mφ are more abundant in the aortic arches of *Saa3*$^{-/-}$ mice compared to WT
291 mice (Fig. 3b). Trem2^{hi} Mφ is previously identified as lipid-laden foam cells within
292 atherosclerotic lesions, underscoring their capacity for lipid processing and
293 phagocytosis [9, 10, 35]. They are associated with anti-inflammatory responses,
294 which may help prevent the establishment of a proinflammatory environment within
295 the plaque [9, 35, 44]. Similar to previous findings, Trem2^{hi} Mφ expresses high *Spp1,*
296 a gene associated with fibrotic responses indicative of tissue repair mechanisms [45,
297 46] (Fig. 3c, Supplementary Fig. 2a). Additionally, this subset expresses *Gpnmb*, a
298 gene implicated in anti-inflammatory processes [29, 47], along with *Fabp5*, which is
299 involved in the uptake and transport of fatty acids [28] (Fig. 3c). Notably, enzymes
300 such as *Lpl*, central to lipid metabolism[48] , and *Mmp12*, a contributor to

301 extracellular matrix remodeling [49], further characterize this population (Fig. 3c).
302 Hence, these data indicate that *Saa3*$^{-/-}$ mice exhibit higher compositions of aortic
303 macrophages with tissue-repairing and anti-inflammatory properties, leading to
304 reduced aortic plaque progression.
305

306 ***Saa3* modulates aortic macrophage functionalities during atherosclerosis**

307 Investigating the transition of macrophage phenotypes from M1-like to M2-like as a
308 therapeutic strategy recognizes the complexity of aortic macrophage phenotypes in
309 atherosclerosis, which extend beyond conventional M1 and M2 polarization states [8,
310 35]. We use typical markers for Chemokine, Interferon (IFN), Inflammatory, and
311 Type II responses to visualize the aortic macrophage subsets from WT and *Saa3*$^{-/-}$
312 mice (Fig. 3d). Among the comparisons between WT and *Saa3*$^{-/-}$ aortic Mφ,
313 pronounced differences were noted in the increased expression levels of chemokines
314 including *Cxcl1*, *Ccl2*, *Ccl3*, and *Ccl4* in *Saa3*$^{-/-}$ than WT Folr2^{hi} Mφ (Fig. 3d).
315 Chemokines are signaling molecules that attract various types of immune cells to sites
316 of infection or injury. Increased expression of chemokines by tissue-resident
317 macrophages enhances the recruitment of neutrophils and lymphocytes, which is
318 crucial for initiating and sustaining an effective immune response [50]. Additionally,
319 there was a higher expression of type II response markers including *Cd163, Mrc1*, and
320 *Msr1* [51-54] in *Saa3*$^{-/-}$ than WT Folr2^{hi} Mφ (Fig. 3d). Moreover, Il10ra showed
321 higher expression in *Saa3*$^{-/-}$ than WT Cd74^{hi}MHCII^{hi} Mφ, and Il10ra is required for
322 protection against atherosclerosis in low-density lipoprotein receptor knockout mice
323 [55]. Furthermore, we observed higher expression levels of interferon regulatory and
324 downstream markers such as *Irf5*, *Irf7*, *Isg15*, and *Stat1* in WT than *Saa3*$^{-/-}$

325 Retnla^{hi}Ear2^{hi} Mφ (Figure 3d), which may indicate an enhanced interferon response in
326 these cells [56, 57]. These expression patterns indicate a significant alteration in gene
327 expression profiles and macrophage composition between the two genotypes,
328 suggesting that deletion of the *Saa3* may modulate macrophage recruitment, type 2
329 immune responses, and inflammatory/anti-inflammatory phenotypes.
330
331 ***Saa3* modulates aortic macrophage communications that impact inflammatory**
332 **processes**
333 To determine the role of *Saa3* in aortic macrophage communication during
334 atherosclerosis, we also performed a comparative analysis of cell interactions using
335 *CellChat* [27] in both WT and *Saa3*$^{-/-}$ macrophages. Our findings indicate a
336 substantial decline in intercellular communication in *Saa3*$^{-/-}$ macrophages, with
337 interaction events decreasing from 482 in WT to 290 in *Saa3*$^{-/-}$ cells (Fig. 3e).
338 Correspondingly, we observed a significant drop in the strength of these interactions,
339 with the average interaction strength in WT macrophages being 17.997 compared to a
340 lower average of 14.348 in *Saa3*$^{-/-}$ macrophages, mirroring the decrease in the number
341 of interaction events (Fig. 3e).
342 The heatmap depicts the overall signaling patterns observed in various macrophage
343 subpopulations from WT and *Saa3*$^{-/-}$ mice (Fig. 3f), and the bar graph shows the
344 relative information flow of these signaling pathways between WT and *Saa3*$^{-/-}$
345 macrophages (Fig. 3g). In the context of inflammatory-mediated atherosclerosis
346 progression, WT macrophages present higher signaling activity in THBS, ANGPTL,
347 LAMININ, PVR, CD226, OSM, NOTCH, CADAM, and JAM pathways compared to
348 *Saa3*$^{-/-}$ macrophages (Figs. 3f-3g). In THBS signaling, *Thbs1* is a critical regulator of
349 macrophage interleukin-1β (IL-1β) production and activation via CD47, highlighting

350 the complex interplay between thrombospondins and immune modulation [58]. In
351 ANGPTL signaling, ANGPTL2 promotes vascular inflammation and accelerates
352 atherosclerosis progression, with increased cardiac ANGPTL2 production linked to
353 heart failure and pathological cardiac remodeling by influencing inflammatory
354 responses and affecting both cardiomyocytes and macrophages[59, 60]. In LAMININ
355 and JAM signaling, LAMININ and junctional adhesion molecules (JAM) are
356 involved in monocyte-to-macrophage differentiation and macrophage migration,
357 playing roles in immune cell dynamics and atherosclerotic disease modulation [61,
358 62]. PVR significantly contributes to atherosclerosis by facilitating leukocyte
359 migration across the endothelium, thereby promoting inflammation [63]. When loss of
360 CD226, a costimulatory molecule, has been observed to protect against
361 atherosclerosis by preventing foam cell formation and reducing plaque buildup [64].
362 Oncostatin M (OSM) signaling promotes atherogenesis and plaque vulnerability by
363 promoting the differentiation of vascular smooth muscle cells into osteoblastic
364 phenotypes via M1 macrophages, potentially leading to plaque instability [35].
365 NOTCH signaling plays a significant role in atherosclerosis development, with *Notch-*
366 *1* deletion inducing anti-inflammatory M2 effects through the PI3K-Akt pathway,
367 contrasting with its increased presence in vulnerable human plaques [65].
368 In contrast to their WT counterparts, *Saa3*$^{-/-}$ macrophages exhibit elevated
369 expression of signaling molecules such as COLLAGEN, GRN, SN, TGFb, and
370 CLEC. Collagen plays a crucial role in modulating macrophage functions and
371 improving plaque stability, with an increased presence in M2-polarizing macrophages
372 within the plaque [66, 67]. GRN exerts anti-atherogenic effects by enhancing nitric
373 oxide production in endothelial cells through the Akt/eNOS signaling pathway,
374 forming a complex with apolipoprotein A-I to stabilize atherosclerotic plaques. In

375 addition, in atherosclerotic mice, its deficiency leads to increased expression of
376 adhesion molecules and inflammatory cytokines [68-70]. TGF-β signaling contributes
377 to the reduction and stabilization of atherosclerotic plaques by altering macrophage
378 functions, and its overexpression is linked to smaller lesions, increased collagen
379 deposition, smooth muscle cell infiltration, and reduced macrophage presence,
380 ultimately fostering a more stable lesion phenotype [71]. CLEC signaling, specifically
381 through Clec4a2, a C-type lectin receptor, protects against atherosclerosis by
382 promoting homeostatic functions within the vessel wall, enhancing cholesterol
383 metabolism, and limiting immune responses to toll-like receptors [72]. In summary,
384 this analysis confirms that aortic macrophages in WT mice are more associated with
385 inflammatory and migration processes, whereas aortic macrophages in *Saa3*$^{-/-}$ mice
386 are more related to vascular protection and aortic plaque stabilization.
387

388 **Differential effects of *Saa3* deficiency on macrophage subpopulations and ligand-**
389 **receptor interactions**

390 We further investigated the differential effects of *Saa3* deficiency on five
391 macrophage subpopulations. Our observations revealed that, aside from Trem2^{hi} Mφ,
392 the gene expression profiles of CD74^{hi}MHCII^{hi} Mφ, Folr2^{hi} Mφ, Retnla^{hi}Ear2^{hi} Mφ,
393 and Apbb2^{hi} Mφ in *Saa3*$^{-/-}$ mice exhibited substantial downregulation of numerous
394 genes when compared to their WT counterparts (Figs. 4a-4d). We also performed GO
395 term enrichment pathway analysis on the downregulated DEGs in these four *Saa3*$^{-/-}$
396 macrophage subpopulations compared to WT (Figs. 4e-4h). The analysis revealed
397 common downregulated genes in *Saa3*$^{-/-}$ mice, including *Lyz1*, *Lyz2*, other lysozyme-
398 related genes, *Cxcl13*, and *Ccl8*, which are associated with pathways involved in cell
399 killing and the destruction of other organisms, suggesting that the absence of *Saa3*

400 impairs macrophage functions in combating pathogens as previous studies [73, 74]
401 (Figs. 4e-4h). Specifically, Folr2^{hi} Mφ in *Saa3*$^{-/-}$ mice showed significant
402 downregulation of *Cxcl13* (Fig. 4b). Previous study indicates patients with carotid
403 atherosclerosis exhibit elevated plasma levels of CXCL13, especially in symptomatic
404 cases, and higher CXCL13 expression within atherosclerotic carotid plaques
405 compared to non-atherosclerotic vessels [75]. CCL8 is a potent chemoattractant for
406 monocytes and macrophages, directing them to areas of inflammation and infection
407 [76, 77]. Retnla^{hi}Ear2^{hi} Mφ in WT mice show higher enrichment in ERK1 and ERK2
408 cascade, positive regulation of angiogenesis, and lipid storage (Figs. 4c, 4g). ERK1
409 and ERK2 signaling pathways regulate macrophage function in atherosclerosis.
410 Deletion of *Erk1* reduces macrophage migration and plaque lipid content in LDL
411 receptor-deficient mice on a high-fat diet [78, 79]. Apbb2^{hi} Mφ in WT mice enrich in
412 defense response to virus and interferon (Figs. 4d, 4h). This may indicate that Apbb2^{hi}
413 Mφ in WT mice has more inflammatory response features than in *Saa3*$^{-/-}$ mice,
414 contributing to chronic inflammation, plaque instability, and progression [80]. To
415 elucidate the specific ligand-receptor interactions contributing to the observed
416 differences in pathway patterns between *Saa3*$^{-/-}$ and WT groups, we conducted a
417 comparative analysis of ligand-receptor signaling within five subpopulations of
418 macrophages (Supplementary Figs 3a-3e). The analysis encompassed an assessment
419 of the differential expression of ligands and receptors and the computation of
420 interaction probabilities, thereby enabling the dissection of signaling discrepancies
421 between the two genotypic conditions. Since aortic Trem2^{hi} Mφs are more abundant
422 in *Saa3*$^{-/-}$ mice, we focus on ligand-receptor interactions within Trem2^{hi} Mφ under
423 both WT and *Saa3*$^{-/-}$ conditions (Supplementary Fig. 3d). Prominently, pairs such as
424 Spp1-Cd44 and Spp1-integrins (Itgav+Itgb1, Itga5+Itgb1, Itga4+Itgb1), exhibit a

425 heightened probability of interaction in the signal transduction pathways of Trem2^{hi}
426 Mφ within the *Saa3*$^{-/-}$ mice (Supplementary Fig. 3d). Spp1 is established to bind
427 integrins Itgav, Itgb1, Itgb5, and Itga4 (Col4a2-Sdc44, Col4a2-Cd44, Col4a2-
428 (Itga9+Itgb1), Col4a1-Sdc44, Col4a1-Cd44, Col4a1-(Itga9+Itgb1)), influencing
429 cellular adhesion and migration crucially [81, 82] (Supplementary Fig. 3d).
430 Furthermore, interactions involving Col4a2 and Col4a1 with their partners are
431 exclusively observed in the *Saa3*$^{-/-}$ condition (Supplementary Fig. 3d). As major
432 constituents of the basement membrane, type IV collagen may have implications for
433 the stability of atherosclerotic plaques [83]. In contrast, the CCL-CCR signaling axis,
434 encompassing Ccl9-Ccr1, Ccl8-Ccr1, Ccl7-Ccr1, Ccl6-Ccr2, Ccl6-Ccr1, Ccl3-Ccr5,
435 and Ccl3-Ccr1, is exclusively active in the WT condition within Trem2^{hi} Mφ
436 transitioning to Retnla^{hi}Ear2^{hi} Mφ (Supplementary Fig. 3d). These chemokine-
437 mediated communications facilitate the recruitment of macrophages or monocytes to
438 sites of inflammation, contributing to the formation and progression of atherosclerotic
439 lesions and plaque vulnerability [84, 85]. Parallel observations were noted for the
440 ligand-receptor pairs Cd74^{hi}MHCII^{hi} Mφ, Folr2^{hi} Mφ, Retnla^{hi}Ear2^{hi} Mφ, and Apbb2^{hi}
441 Mφ to Retnla^{hi}Ear2^{hi} Mφ (Supplementary Figs. 3a-3e). It is posited that these altered
442 signaling patterns may underlie the observed reductions in plaque burden and
443 macrophage recruitments in *Saa3*$^{-/-}$ mice.
444
445 **Trem2^{hi} Mφ potentially mitigates aortic plaque development by enhancing lipid**
446 **uptake, promoting an anti-inflammatory environment, and increasing tissue**
447 **remodeling.**
448 In atherosclerosis, *Saa3* deletion precipitates substantial changes in macrophage gene
449 expression profiles, within the Trem2^{hi} Mφ, as evidenced by differential expression

450 between WT and *Saa3*$^{-/-}$ groups (Fig. 5a). The upregulation of genes in *Saa3*$^{-/-}$ than
451 WT Trem2^{hi} Mφ such as *Fabp4, Fabp5,* and *Lpl*, which are central to lipid
452 metabolism [86, 87], as well as *Ctsk*, has been implicated in promoting disturbed
453 flow-induced endothelial inflammation [88]. Other genes including *Gpnmb,*
454 *Atp6v0d2, Mrc1, Mmp12*, and *Spp1* also exhibit altered expression (Fig. 5a). Studies
455 suggest that *Gpnmb* may be anti-inflammatory by promoting inflammation resolution,
456 as it can attenuate pro-inflammatory responses and promote M2 polarization in
457 macrophages [47, 89, 90]. The suppression of *Gpnmb* has been associated with
458 enhanced atherosclerotic plaque formation, whereas its overexpression correlates with
459 decreased plaque development [91]. Augmented *Atp6v0d2* expression activates
460 autophagy as a compensatory response to hemodynamic pressure, which indicates its
461 role in maintaining plaque stability and potentially curtailing the progression of
462 atherosclerosis [92, 93]. *Mrc1* appears to modulate macrophage polarization toward
463 an anti-inflammatory phenotype [94], while *Mmp12* plays a pivotal role in attenuating
464 inflammation and fostering resolution via targeted proteolysis of chemokines [95, 96].
465 Spp1+ foamy macrophages have been linked to signaling pathways that might abate
466 plaque progression and stabilize susceptible lesions [97]. These genes correspond to
467 GO enrichment pathways such as lipid localization, fatty acid transport, and the
468 positive regulation of macrophage-derived foam cell differentiation (Fig. 5b). These
469 results suggest that *Saa3*$^{-/-}$ Trem2^{hi} Mφ may possess enhanced lipid uptake and
470 metabolism capabilities, which could contribute to the significant reduction in plaque
471 size. Additionally, genes like *Ctsk*, *Gpnmb*, *Igf1*, and *Spp1* are associated with tissue
472 remodeling pathways, indicating a potential shift of *Saa3*$^{-/-}$ Trem2^{hi} Mφ towards an
473 anti-inflammatory phenotype (Fig. 5b). Differential gene expression analysis utilizing
474 violin plots demonstrated that genes associated with tissue repair and lipid

475 metabolism—specifically *Gpnmb*, *Fabp5*, *Lpl, Lgals3*, *Cd36*, *Spp1*, and *Pparg*—are
476 more prominently expressed in *Saa3*$^{-/-}$ Trem2^{hi} Mφ compared to their WT
477 counterparts (Fig. 5c). CD36 is a scavenger receptor widely expressed on the surface
478 of various cell types, including macrophages. CD36 binds to oxLDL particles,
479 facilitating their uptake into the macrophage, particularly in the context of
480 atherosclerosis and inflammation [98]. Concomitantly, there is a downregulation of
481 genes in *Saa3*$^{-/-}$ than WT Trem2^{hi} Mφ such as *Thbs1, Kdm7a, Vegfa, Slc7a11, Fn1*,
482 and *Chil3*. These genes correspond to GO enrichment pathways such as positive
483 regulation of chemotaxis, positive regulation of vasculature development, and
484 angiogenesis (Fig. 5b). Angiogenesis is associated with inflammatory cells and can
485 contribute to plaque instability [99, 100]. This complex gene expression network
486 underscores the multifaceted influence of *Saa3* in atherosclerosis and pinpoints
487 interconnected genes geared toward modulating macrophage function to combat
488 disease progression.
489 Analysis of aortic Trem2^{hi} macrophages from WT and *Saa3*$^{-/-}$ mice also revealed a
490 consistent expression pattern for a cohort of genes associated with lipid metabolism
491 and cholesterol processing (Figs 5b-5c). The violin plots compare the expression
492 levels of genes central to cholesterol efflux pathways, including *Abca1, Abcg1,*
493 *Nr1h2, Scarb, Nr1h3*, and *Apoe* (Fig. 5c, Supplementary Fig. 4). There were no
494 statistically significant differences observed between the two genotypes for most
495 genes (Fig. 5c).
496 Analysis through *CellChat* has additionally revealed alterations in the growth
497 differentiation factor (GDF) signaling pathway in all subsets of the aortic
498 macrophages (Figs. 5d-5e). In the *Saa3*$^{-/-}$ Trem2^{hi} macrophage phenotype, there is a
499 notable shift towards the sender role in the GDF signaling network (Fig. 5d). In

500 contrast, Folr2^{hi} macrophages predominantly assume the signaling initiative in the
501 WT condition (Figs. 5d-5e). This shift in signaling behavior suggests that the absence
502 of *Saa3* leads to a reprogramming of the Trem2^{hi} macrophage population, endowing
503 them with a more prominent role in initiating signaling within the GDF pathway.
504 GDF-15 has been reported to reduce cardiac damage and rupture after myocardial
505 infarction by mitigating inflammation and apoptosis via the PI3K/Akt pathway. It also
506 protects against atherosclerosis by modulating apoptosis, inhibiting monocyte
507 recruitment and macrophage activation, and enhancing plaque stability [101-103].
508 Other studies suggest GDF-15 may reduce macrophage accumulation in *Ldlr*$^{-/-}$ or
509 *Apoe*$^{-/-}$ mice [104-106]. This shift in the gene expression landscape highlights the
510 critical role of *Saa3* in regulating macrophage function and may provide insight into
511 the molecular mechanisms underpinning the immune responses in aortic plaque
512 progression.
513
514 **SAA3 modulates cholesterol efflux, synthesis, and inflammatory responses in**
515 **macrophages under steady-state condition or during foamy macrophage**
516 **differentiation**
517 SAA3 has been shown to exacerbate atherosclerosis in *ApoE*$^{-/-}$ mice, as evidenced by
518 increased lesion area upon overexpression and reduced disease severity with
519 suppression [20]. Another study also observed reduced aortic plaque lesions in
520 atherosclerotic *Saa3*$^{-/-}$*Ldlr*$^{-/-}$ mice and indicated that these effects are sex-dependent
521 [14]. To validate our scRNA-seq observations on aortic macrophages and investigate
522 the role of *Saa3* in foamy macrophages, we performed qRT-PCR to assess the
523 expression of inflammatory genes (*Il1b* and *Tnf*), cholesterol efflux genes (*Abca1* and
524 *Abcg1*), and cholesterol synthesis genes (*Cyp51* and *Hmgcr*) in bone marrow-derived

525 macrophages (BMDMs) from WT and *Saa3*$^{-/-}$ mice (Fig. 6a). These BMDMs were
526 treated overnight with either media alone or 20 µg/ml soluble cholesterol to
527 differentiate cells into foamy macrophages (Fig. 6a). We also conducted scRNA-seq
528 analysis on WT BMDMs treated with SAA3 in either media alone or 20 µg/ml
529 soluble cholesterol (Fig. 6a). Overall, gender-specific effects were generally minimal
530 under these experimental conditions, while genes involved in cholesterol efflux and
531 synthesis were significantly lower in female WT foamy macrophages treated with
532 SAA3 compared to males (Figs. 6b-c). Consistent with the previous study [14], *Il1b*
533 expression was significantly upregulated in BMDMs from female *Saa3*$^{-/-}$ mice
534 compared to WT under media-alone conditions, with no such effect observed in male
535 mice, while *Tnf* expression remained unchanged between genotypes (Fig. 6b).
536 Following soluble cholesterol treatment, both WT and *Saa3*$^{-/-}$ BMDMs present
537 minimal differences, with upregulated expression of the cholesterol efflux gene
538 (*Abca1*) and downregulated expression of the cholesterol synthesis gene (*Cyp51*),
539 indicative of the foamy macrophage phenotype (Fig. 6c). SAA3 treatment
540 significantly reduced cholesterol efflux gene expression (*Abca1* and *Abcg1*) while
541 increasing cholesterol synthesis gene expression (*Hmgcr*) in WT BMDMs undergoing
542 foamy macrophage differentiation (Fig. 6c). We next performed scRNA-seq analysis
543 on SAA3-treated WT BMDMs to confirm that genes associated with tissue repair and
544 lipid metabolism (*Gpnmb*, *Lpl*, *Lgals3*, *Spp1*, *Cd36*, *Pparg*) were significantly
545 downregulated compared to untreated controls (Fig. 6d). This aligns with the *in vivo*
546 phenotypes, where Trem2^{hi} aortic macrophages from *Saa3*$^{-/-}$ mice exhibited
547 significantly higher expression of these genes compared to Trem2^{hi} macrophages
548 from WT mice (Figs. 5c, 6d). We further observed the genes associated with acute
549 inflammatory response, interferon responses, and cell chemotaxis are increased in

550 SAA3-treated WT BMDMs (Figs. 6e-6f). Notably, exogenous SAA3 significantly
551 increases *Il1b* expression in both foamy and non-foamy macrophages (Fig. 6b).
552 These data indicate that SAA3 modulates inflammatory and lipid metabolism
553 pathways in macrophages, particularly during foamy macrophage differentiation, by
554 reducing cholesterol efflux, increasing cholesterol synthesis, and enhancing
555 inflammatory and interferon responses, suggesting that SAA3 potentially exacerbates
556 atherosclerosis progression through these mechanisms.
557

558 **Discussion**

559 Gut microbiota plays significant roles in inducing and maintaining sex dimorphism,
560 particularly in relation to immune responses, metabolism, and hormone regulation. In
561 NOD mice, the sex difference in type 1 diabetes susceptibility disappears under germ-
562 free conditions, while gut microbiota transfer from males to females elevates
563 testosterone levels and protects against disease [107]. This protection, mediated by
564 microbiota-regulated sex hormones, is lost upon androgen receptor blockade[107].
565 Metabolic syndrome is also mediated by the gut microbiota in a sex-dependent
566 manner, as demonstrated by the transfer of this sex-specific effect through fecal
567 transplantation between male and female mice, with antibiotic treatment eliminating
568 these differences and highlighting the causative role of microbiota in sexual
569 dimorphism [108]. Furthermore, the microbiota regulates bone marrow mesenchymal
570 stem cells (BMMSCs) by inhibiting osteogenesis and promoting adipogenesis, as
571 shown by increased osteogenic differentiation in germ-free (GF) mice, while
572 colonization with specific-pathogen-free (SPF) microbiota restored normal BMMSC
573 proliferation, differentiation, and immunomodulatory functions [109]. The microbiota
574 regulates hematopoietic stem cell (HSC) self-renewal and differentiation under stress

575 by modulating local bone marrow iron availability through red blood cell recycling by
576 macrophages [110]. Notably, the gut microbiota modulates the expression of SAA3 in
577 colonic and adipose tissue via Toll-like receptor signaling [15]. These findings
578 suggest that the gut microbiota may influence confounding factors, such as iron
579 availability and SAA3 levels, within the tissue microenvironment, thereby affecting
580 sex dimorphism and immune cell differentiation. The SAA3-induced sex dimorphism
581 observed in previous studies may also be influenced by microbiota-driven effects on
582 bone marrow cell differentiation during early life.
583 Previous study indicates that SAA3 promotes atherosclerosis in male mice while
584 providing protective effects in female mice [14]. Jylhava et. al. suggest a potential
585 sex-dimorphism in the relationship between serum amyloid A (SAA) and early
586 atherosclerosis, as SAA levels correlated with carotid intima-media thickness (IMT)
587 in men but not in women, indicating differing underlying mechanisms of
588 atherosclerotic risk between the sexes [111]. The absence of SAA3 in female mice led
589 to a significant decrease in adipose tissue macrophage content and inflammation,
590 while similar effects were not observed in male mice [112]. Another study highlights
591 a significant sex dimorphism in the association between SAA levels and adipocyte
592 size, with pronounced correlations observed in lean and overweight women, while no
593 such associations were found in men [113]. Our results indicate there is still less
594 aortic plaque progression in female atherosclerotic *Saa3*$^{-/-}$ than in WT mice (Fig. 1).
595 The gender differences were minimal but SAA3 significantly reduced cholesterol
596 efflux genes and increased synthesis genes, particularly in female WT foamy
597 macrophages (Fig. 6). SAA3-treated WT BMDMs showed downregulation of tissue
598 repair and lipid metabolism genes and upregulation of acute inflammatory and
599 interferon-response genes, aligning with *in vivo* phenotypes of Trem2^{hi} macrophages

600 in *Saa3*$^{-/-}$ mice represented the higher expression of lipid metabolism genes (Fig. 6).
601 These results suggest that SAA3 modulates inflammatory and lipid pathways in
602 foamy macrophages, which may be exacerbating atherosclerosis progression *in vivo*.
603 The single-cell RNA sequencing (scRNA-seq) analysis of CD45+ cells from aortic
604 arches revealed significant alterations in the aortic immune cell landscape of *Saa3*$^{-/-}$
605 mice. Increased proportions of T cells, B cells, monocytes, and γδ T cells were noted,
606 while macrophages and innate lymphoid cells (ILCs) were reduced compared to WT
607 mice (Fig. 2). This shift in immune cell composition suggests that *Saa3* deficiency
608 alters the inflammatory responses within the aortic arches, potentially contributing to
609 the observed reduction in plaque progression. *CellChat* analysis further highlighted
610 the impact of *Saa3* deficiency on intercellular communication within the aortic
611 microenvironment (Figs. 2, 3). *Saa3*$^{-/-}$ mice exhibited enhanced intercellular
612 interaction strength, particularly among γδ T cells and all other immune cell types,
613 suggesting a more reactive immune milieu. Conversely, the reduced macrophage-to-
614 all other immune cell signalings were observed, indicating a dampened inflammatory
615 response (Fig. 2). These findings suggest that *Saa3* deficiency promotes shifts towards
616 reparative and less inflammatory phenotypes in aortic immune cells, potentially
617 influencing atherosclerosis progression.
618 Compared to our previously published dataset, where we profiled single-cell sorted
619 *Cx3cr1*-derived aortic macrophages during atherosclerosis progression and regression
620 [8], we identified 11 aortic macrophage clusters, while we only identified five distinct
621 clusters with notable differences in gene expression between WT and *Saa3*$^{-/-}$ mice
622 (Fig. 3a). This may be due to the difference in the platform used to capture single cells
623 between 10X Genomics and BD Rhapsody. Nonetheless, we still observed that
624 Trem2^{hi} macrophages were more abundant in *Saa3*$^{-/-}$ mice (Fig. 3b) and revealed gene

625 expression profiles indicative of enhanced lipid metabolism and tissue repair
626 functions (Fig. 5). These macrophages may be crucial in mitigating plaque
627 progression by promoting an anti-inflammatory environment and enhancing
628 extracellular matrix production. Our findings also highlight the differential ligand-
629 receptor interactions in WT and *Saa3*$^{-/-}$ mice macrophages (Supplementary Fig. 3).
630 *Saa3* deficiency led to altered signaling dynamics, particularly in Trem2^{hi}
631 macrophages, which showed increased interactions involving *Spp1* and integrins, as
632 well as type IV collagen, suggesting enhanced adhesion and migration capabilities. In
633 contrast, chemokine-mediated communications were more prominent in WT
634 macrophages, facilitating the recruitment of inflammatory cells to atherosclerotic
635 lesions (Supplementary Fig. 3d). The observed changes in gene expression and
636 intercellular communication underscore the complex role of *Saa3* in modulating
637 Trem2^{hi} macrophage functions during atherosclerosis. *Saa3* deficiency appears to
638 shift Trem2^{hi} macrophages towards a phenotype that promotes tissue repair and
639 plaque stability (Fig. 5), which may explain the reduced plaque progression despite
640 elevated cholesterol levels.
641 In conclusion, our study reveals that *Saa3* deficiency has a dual impact on
642 atherosclerosis, reducing aortic plaque progression in female mice while increasing
643 peripheral lipid levels. The enhanced reparative and anti-inflammatory properties of
644 macrophages in *Saa3*$^{-/-}$ mice likely contribute to the observed protective effects
645 against atherosclerosis. *Saa3* is exclusively expressed in macrophages within the
646 immune cell population and SAA3 modulates inflammatory and lipid pathways in
647 foamy macrophages. These findings provide valuable insights into the regulatory
648 mechanisms of immune function within the aortic niche and highlight the potential of
649 targeting *Saa3* for therapeutic strategies in atherosclerosis. Further research is

650 warranted to elucidate the precise molecular pathways involved and to explore the
651 therapeutic potential of modulating *Saa3* expression in cardiovascular diseases.
652 The observed alterations in immune cell composition and intercellular communication
653 in *Saa3*-deficient mice highlight a shift toward reparative and anti-inflammatory
654 phenotypes, potentially stabilizing plaques despite elevated cholesterol levels.
655

656 **Author contributions**

657 TYC, YZY, and JDL designed experiments and interpreted the data. TYC and YZY
658 wrote the manuscript draft, followed by JDL editing. TYC, YZY, CJL, JCW, CHY,
659 YTC, and PAC performed experiments. TYC and YZY coordinated and performed
660 the single-cell RNA-seq experiments and then analyzed single-cell RNA-seq data.

661

662 **Acknowledgments**

663 We thank the Animal Resource Center and the Consortium of Integrative Biomedical
664 Science Key Technology at National Taiwan University for their technical support.
665 We also acknowledged the AAV Core Facility of Academia Sinica in generating
666 recombinant AAV (Grant AS-CFII112-204) and National Center for High-
667 performance Computing (NCHC) of National Applied Research Laboratories
668 (NARLabs) in Taiwan for providing computational and storage resources. Funding:
669 This work was financially supported by the National Science and Technology
670 Council, Taiwan (110-2636-B-002-021, 111-2636-B-002-024, 112-2636-B-002-015,
671 113-2636-B-002-009), National Taiwan University (113L894501, 113-UN0066),
672 Ministry of Education (Yushan Young Fellow Program, Featured Areas Research
673 Center Program of "Center for Advanced Computing and Imaging in Biomedicine"
674 (NTU-113L900701))

675 **Material and Methods**

676

677 **Animals**

678 All animal procedures were approved by the National Taiwan University IACUC
679 Committee. The Saa3-knockout mice (*Saa3*$^{-/-}$; C57BL/6N-
680 Saa3tm1.1(KOMP)Vlcg/MbpMmucd) were developed by the Mutant Mouse
681 Resource & Research Centers (MMRRC). The ES cell clone 13807A-A1 was injected
682 into morulae or blastocysts to generate chimeric mice. These chimeras were then bred
683 with C57BL/6N mice, resulting in the production of heterozygous tm1 (Deletion)
684 mice. To achieve recombination at the LoxP sites, heterozygous tm1 mice were
685 crossed with a ubiquitous Cre deleter mouse line, generating tm1.1 (CRE-mediated
686 Deletion) allele mice. Notably, the archived germplasm does not carry the Cre
687 transgene. Cryo-recovery of the strain will be conducted using C57BL/6N females by
688 the MMRRC. Detailed information about the Cre-mediated deletion process can be
689 found at the following reference: Velocigene KOMP Repository, clone 13807,
690 http://velocigene.com/komp/detail/13807. The cryopreserved sperm were acquired
691 and recovered by the National Laboratory Animal Center in Taiwan. We generated
692 heterozygous *Saa3*$^{+/-}$ mice and bred them to obtain 12-week-old Wild-type C57BL/6J
693 mice wild-type (WT) and *Saa3*$^{-/-}$ littermates used for the experiments. Murine
694 atherosclerosis was induced by injecting intraperitoneally once with AAVmPCSK9
695 (ssAAV8/hAAT-mPCSK9D377Y, AAV core, Institute of Biomedical Sciences,
696 Academia Sinica, using a plasmid acquired from Addgene (Plasmid #58376) and
697 kindly provided by Dr. Mi-Hua Tao) at 5×10^{11} viral particles/mouse and fed on
698 Western diet (Research Diets, Cat# D12079Bi) for 18 weeks. All mice were housed in
699 a specific pathogen-free (SPF) environment within individually ventilated cages

700 (IVC) at a ventilation rate of 70-100 air changes per hour (ACH) under positive
701 pressure. The facility maintained a constant temperature of 22 ± 2°C and a relative
702 humidity of 55 ± 10%. A 12-hour light-dark cycle was regulated by timers (7:00 AM
703 to 7:00 PM light, 7:00 PM to 7:00 AM dark).
704

705 **Cholesterol level measurements**

706 Blood samples were collected from mice and total cholesterol levels in plasma were
707 assessed in WT and *Saa3*$^{-/-}$ mice subjected to AAVmPCSK9D377Y and fed on
708 Western Diet for 0, 4, 8, 12, and 16 weeks (n=5 mice per group). Cholesterol levels
709 were measured using a colorimetric assay (FUJIFILM/Wako, Cat# 639-50981), with
710 absorbance read at 600 nm following a 5-minute incubation at 37 °C. HDL and
711 LDL/VLDL cholesterol levels in plasma were quantified using the ab65390
712 Cholesterol Assay Kit (Abcam, Version 13a, Updated 17 April 2023), following the
713 manufacturer's protocol with adaptations for our setup. Plasma (20-30 µL) was mixed
714 with an equal volume of 2X Precipitation Buffer to separate the HDL and LDL/VLDL
715 cholesterol fractions. After adding reaction mixes, samples were incubated at 37 °C
716 for 60 minutes away from light. Absorbance was measured at 570 nm using a
717 microplate reader, and cholesterol concentrations were determined by correlating
718 absorbance readings with the standard curve. Statistically significant differences
719 between the two groups at respective time points were determined using the unpaired
720 Mann-Whitney U-test (*$p < 0.05$).
721

722 **Histology**

723 At harvesting, the aortic arch was meticulously excised from the experimental mice
724 for the subsequent single-cell isolation, and then aortic roots were embedded in OCT
725 (Catalog # NC0696746). Serial sections were performed at 6 μm on embedded aortic
726 roots and stained with Oil Red O solution (Sigma) for 10 minutes at 37°C. Intimal
727 lesions and stained areas were imaged by an inverted fluorescence microscope
728 (OLYMPUS CKX53) and quantified by ImageJ [17].
729

730 **Aortic cells flow cytometry sorting and single-cell RNA-seq library preparation**

731 The protocol for isolating aortic cells from mice is as previously described[8]. Briefly,
732 the procedure began with aorta perfusion using phosphate-buffered saline (PBS).
733 After perfusion, the aortas were stored in FACS buffer (1X HBSS, 1% BSA, 1mM
734 EDTA, 20mM HEPES, and 1mM Sodium Pyruvate). The enzymatic digestion
735 processes involved immersing the aorta in a digestion buffer containing 4U/ml
736 liberase (Roche, Cat. 54001127001), 100 ug/ml hyaluronidase (Sigma, Cat. H3506),
737 and 100 ug/ml DNase I (Sigma, Cat. DN25), followed by fine mincing. The mixture
738 was incubated at 37°C to facilitate effective digestion, with the process repeated 5-6
739 times to ensure complete tissue breakdown. After digestion, the mixture was filtered
740 through a 35μm strainer to obtain a single-cell suspension. The collected cells were
741 then stained with CD45 (Alexa Fluor 488 anti-mouse CD45, Clone: 30-F11,
742 Biolegend, Cat. 103122) and Live/Dead (L/D) Blue markers (Thermo Fisher, Cat.
743 L34962), and the CD45-positive, L/D Blue-negative cells were sorted as
744 Supplementary Figure 1 to prepare single-cell libraries.

745 Single-cell samples were labeled using the BD™ Mouse Immune Single-Cell
746 Multiplexing Kit (Cat. 633793) for each cartridge run on the BD Rhapsody Express
747 Single Cell Analysis System for single-cell capture, followed by cDNA synthesis with
748 the BD Rhapsody cDNA Kit (Cat. 633773). The mRNA Whole Transcriptome
749 Analysis (WTA) and Sample Tag libraries were prepared using the BD Rhapsody™
750 WTA Amplification Kit (Cat. 633801), according to the manufacturer's guidelines.
751 The quality and quantity of the libraries were assessed using the Agilent 4200
752 TapeStation System with Agilent High Sensitivity D1000 ScreenTape (Agilent
753 Technologies, Santa Clara, CA) and a Qubit Fluorometer with the Qubit dsDNA HS
754 Assay (Invitrogen, MA, USA). Finally, the libraries were sequenced using the
755 NovaSeq PE150 sequencer (Illumina, San Diego, CA).

756

757 **Aortic single-cell sequencing data reads alignment and analysis**

758 The fastq files generated from sequencing were processed using Seven Bridges
759 Genomics. The data were aligned to the mouse_GRCm38-PhiX-gencodevM19-
760 20181206 and demultiplexed using hashtags to separate samples. Subsequent steps
761 included filtering low-quality cells and identifying unique molecule identifiers
762 (UMIs) to produce filtered matrices, which were then utilized as inputs for further
763 analysis. The filtered matrices were analyzed using the Seurat package (v.4.3.0)[103] in
764 R (v.4.3.1). Initially, to exclude low-quality cells, we filtered out cells with
765 nFeature_RNA < 200 and percent.mt > 15, tailoring filter parameters for each sample
766 based on violin plots of RNA feature numbers and the percentage of mitochondria in
767 each cell. We used the FindVariableFeatures() function in each sample to select the
768 top 2000 genes with the highest variance using the variance variance-stabilizing

769 transformation (VST) method for downstream analysis. Next, we applied a linear
770 transformation to scale the data, ensuring equal weight to each gene expression level
771 in downstream analysis. A linear dimensional reduction (PCA) was performed, and
772 the Elbow plot was used to decide which PCs to include in the following steps. We
773 cluster cells using the Louvain algorithm (resolution = 0.5). The non-linear
774 dimensional reduction method was employed for visualizing cell clustering, such as
775 UMAP.

776 To analyze two or more single-cell datasets together, we followed the Seurat
777 integration analysis pipeline. We used the FindIntegrationAnchors() function to
778 identify anchors, followed by the IntegrateData() function to use these anchors to
779 integrate the datasets. To automatically annotate cell types, SingleR (v.2.8.0) was
780 utilized with the ImmGen database, which specifically focuses on immunological cell
781 types. To ensure the analysis targeted the immune population, contaminating cell
782 types such as fibroblasts and stromal cells were subsequently excluded. To identify
783 differentially expressed features, we employed the FindAllarkers() or FindMarkers()
784 functions to identify biomarkers for each cell cluster (min.pct = 0.25, logfc.threshold
785 = 0.25). We used visualization tools such as VlnPlot, feature plot, dotplot, and
786 heatmap to display intergroup gene expression differences. Additionally, to
787 comprehend the potential biological pathway connections of gene sets expressed by
788 each cell population and their differences between two genotypes, we conducted a
789 Gene Ontology (GO) analysis using the ClusterProfiler package (v4.8.3)[104]. This was
790 done after identifying differentially expressed genes (DEGs) in each cell population
791 compared to the cell population of another genotype. The results were visualized
792 using a Dotplot. Moreover, the analysis of intercellular communications was
793 conducted using the CellChat package (v1.6.1)[105]. This approach allowed us to

794 understand the roles played by each cell group in signal transduction pathways and
795 compare the differences in cellular signaling among cell groups under different
796 genotypes.

797

798 **Bone marrow-derived macrophages (BMDMs) culture**

799 Bone marrow cells harvested from C57BL/6J mice were cultured in RPMI 1640
800 medium supplemented with 10% heat-inactivated fetal bovine serum (FBS), 1%
801 penicillin/streptomycin/amphotericin B (P/S/A), and 20 ng/mL macrophage colony-
802 stimulating factor (M-CSF). On day 3, the medium was replaced with 10 mL fresh
803 medium. On day 5, an additional 2 mL of medium was added. After seven days of
804 culture, adherent macrophages were detached using Accutase and treated with 100
805 ng/mL SAA3 protein. The cell suspension was adjusted to a density of 5×10^6
806 cells/mL, seeded into a 48-well plate, and cultured for 24 hours.

807

808 **Real-time RT-PCR**

809 Total RNA was extracted from BMDMs using TRIzol™ Reagent, and cDNA was
810 synthesized using SuperScript™ IV Reverse Transcriptase. Real-time RT-PCR was
811 performed with TaqMan™ Fast Advanced Master Mix on a CFX Connect Real-Time
812 PCR Detection System. The assays utilized the following TaqMan probes: *Gapdh*
813 (Mm99999915_g1), *Saa3* (Mm00441203_m1), *Il-1β* (Mm00434228_m1), and *Tnf*
814 (Mm00443258_m1). Additionally, real-time RT-PCR was also conducted using
815 iTaq™ Universal SYBR® Green Supermix with primers targeting *Abca1*, *Abcg1*,
816 *Hmgcr*, and *Cyp51*. The fold change in each target mRNA was determined by
817 normalizing its expression level to *Gapdh* within the same sample. Relative gene
818 expression was calculated using the comparative method ($2^{-\Delta\Delta CT}$).

819

820 **BMDM single-cell RNA library preparation and sequencing**

821 BMDMs were fixed and permeabilized according to the Evercode™ Fixation v2
822 protocol (Parse Biosciences). The split-pool barcoding process, following the
823 Evercode™ WT v2 protocol, consisted of three rounds. In Round 1, cells were
824 distributed into wells, and sample-specific barcodes were applied to the fixed cells
825 using an in-cell reverse transcription (RT) reaction. Cells from all wells were then
826 pooled together. In Round 2, cells were redistributed across a plate, and an in-cell
827 ligation was performed to append the second barcode. The cells from each well were
828 again pooled together. In Round 3, cells were split across a plate, and a third barcode
829 was appended with another in-cell ligation. After pooling cells from each well, the
830 pooled cells were divided across multiple sublibraries. The cells were then lysed, and
831 the library was fragmented, end-repaired, and went through A-tailing followed by the
832 ligation of the sequencing adaptor. The library was then labeled with a fourth
833 sublibrary-specific barcode. The quality of dsDNA libraries was analyzed using the
834 High Sensitivity D5000 ScreenTape Kit (Agilent) and concentrations were assessed
835 with the Qubit dsDNA HS Kit (Thermo Fisher Scientific). Libraries were sequenced
836 on a NovaSeq X Plus (Illumina) with 10% PhiX.

837

838 **BMDM single-cell RNA data processing**

839 The sequencing data was demultiplexed and mapped to database (mm10, GRCm38)
840 with the commercial pipeline (ParseBiosciences-Pipeline.v1.2.1). The sequence reads
841 from different samples was then distributed based on different Round 1 barcode with
842 R(v4.4.2). To exclude low-quality cells, we filtered cells with nFeature_RNA > 200,
843 nFeature_RNA < 2000, and percent.mt < 45, adjusting the filter parameters for each

844 sample based on violin plots of RNA feature counts and mitochondrial percentages
845 per cell. The FindVariableFeatures() function was used to select the top 2000 genes
846 with the highest variance, applying the variance-stabilizing transformation (VST)
847 method for downstream analysis. The data were then scaled using a linear
848 transformation to ensure equal weighting of gene expression levels in subsequent
849 analyses. Principal component analysis (PCA) was performed for linear dimensional
850 reduction, and the Elbow plot was used to determine the number of principal
851 components (PCs) to retain. Cell clustering was conducted using the Louvain
852 algorithm with a resolution of 0.5. For visualization, we applied the non-linear
853 dimensional reduction method UMAP. For integrating two or more single-cell
854 datasets, we followed the Seurat integration analysis pipeline. The IntegrateLayers()
855 function with the CCAIntegration method was used for dataset integration, followed
856 by the JoinLayers() function to merge the layers. Cell types were annotated
857 automatically using SingleR (v2.8.0) with the ImmGen database, which specializes in
858 immunological cell types. Contaminating cell types, such as fibroblasts, were
859 excluded to ensure the analysis focused on the immune population. To identify
860 potential biological pathway connections and differences following SAA3 protein
861 treatment, we performed Gene Ontology (GO) analysis using the ClusterProfiler
862 package (v4.10.1) on differentially expressed genes (DEGs) from BMDMs under
863 different conditions. Results were visualized using DotPlot representations.
864

865 **Data and code availability**

866 Raw sequence data from single-cell RNA sequencing experiments are deposited in the
867 NCBI Sequence Read Archive under BioProject accession number PRJNA1129034
868 and gene expression omnibus (GEO) accession number GSE270922. All processing

869 was performed in R and analysis scripts can be found on Github at

870 (https://github.com/JDLinLab/Saa3KO-Arch-scRNAseq-pepline-)

871

872

873

874 ## Figure legend

875

876 **Fig. 1 Effects of *Saa3* deletion on peripheral lipid profiles and aortic plaque**

877 **progression during atherosclerosis.**

878 **(a)** Schematic of an experimental model for the time points of plasma collections and

879 single-cell RNA sequencing (scRNA-seq) on aortic immune cells. C57BL/6 wild-type

880 (WT) and *Saa3*$^{-/-}$ female mice were injected with AAVmPCSK9 and fed with the

881 Western diet for 18 weeks. Then aortic arches were digested to single-cell

882 suspensions and FACS-sorted aortic CD45+ cells were subjected to scRNA-seq on

883 the BD Rhapsody platform from WT and *Saa3*$^{-/-}$ mice.

884 **(b)** Plasma total cholesterol levels in WT and *Saa3*$^{-/-}$ mice subjected with

885 ssAAV8/hAAT-mPCSK9 and fed with the Western diet for 0, 4, 8, 12, and 16 weeks.

886 **(c)** Measurement of high-density lipoprotein (HDL) cholesterol levels and low-

887 density lipoprotein (LDL) cholesterol levels in plasma from WT and *Saa3*$^{-/-}$ mice over

888 a period of 0, 2, 4, 8, 12, and 16 weeks.

889 **(d)** Representative Oil Red O staining of aortic root sections in WT and *Saa3*$^{-/-}$ mice

890 at 18 weeks post Western diet. Scale bar: 100 μm.

891 **(e)** As in (d), quantification of the lesion area of aortic root sections stained with Oil

892 Red O.

893 All data are presented as mean ± SEM; Statistically significant differences between

894 the two groups at respective time points were denoted by asterisks (*$p < 0.05$),

895 determined using an unpaired Mann-Whitney U-test. Each symbol represents an
896 individual mouse; WT mice (n=5), *Saa3*$^{-/-}$ mice (n=5).
897
898 **Fig. 2 *Saa3* deficiency alters immune intercellular communication in aortic**
899 **arches during atherosclerosis progression.**
900 **(a)** UMAP visualization compares the distribution of cell types in aortic arches
901 between WT and *Saa3*$^{-/-}$ mice. Unbiased cell type annotations against the IMMGEN
902 database are colored and labeled accordingly on the plot.
903 **(b)** Cell type composition by percentages of WT and *Saa3*$^{-/-}$ mice (blue, WT; red,
904 *Saa3*$^{-/-}$) in total sorted CD45+ cells.
905 **(c)** Heatmap of top 5 marker genes of each cell type in aortic arches from WT and
906 *Saa3*$^{-/-}$ mice. The selection of these top marker genes was based on the results of a
907 Wilcoxon test for differential expression.
908 **(d)** Bar plots show the number (left) and strength (right) of inferred interactions of
909 intercellular communication networks in aortic arches from WT and *Saa3*$^{-/-}$ mice.
910 **(e)** Heatmap visualization of intercellular communication networks in aortic arches
911 from WT and *Saa3*$^{-/-}$ mice. The red and blue colors represent increased or
912 decreased signaling in the aortic arches of *Saa3*$^{-/-}$ mice compared to the WT mice. The
913 top-colored bar plot represents the sum of the columns of values (incoming signaling),
914 and the right-colored bar plot represents the sum of a row of values (outgoing
915 signaling).
916 **(f)** Volcano plot illustrating differential gene expression in total macrophages within
917 aortic arches of *Saa3*$^{-/-}$ versus WT mice. The x-axis displays the $\log_2$ fold change,
918 while the y-axis shows the -Log_{10} *p*-value. Grey dots denote genes without significant
919 differences, green dots indicate genes with significant fold changes, and red dots mark

920 genes significant in both fold change and *p*-value. The dashed vertical lines represent
921 the fold change boundaries, and the dashed horizontal line demonstrates the p-value
922 significance threshold.
923 **(g)** Top 10 biological processes enriched in total macrophages within the aortic arches
924 of WT mice compared to *Saa3*$^{-/-}$ mice (upper panel) or *Saa3*$^{-/-}$ mice compared to wild-
925 type mice (lower panel). Enrichment analysis utilized GO pathways to identify
926 significant biological processes. The gene ratio is plotted along the x-axis, and the
927 enriched biological processes are listed on the y-axis. A color gradient has been
928 applied to indicate the -$\log_{10}$ adjusted *p*-value (p.adjust) of each term, with the size of
929 each point reflecting the number of genes associated with the respective pathway.
930
931 **Fig. 3 Delineation of macrophage sub-cluster in aortic arches between WT and**
932 ***Saa3*$^{-/-}$ mice during atherosclerosis progression.**
933 **(a)** UMAP plots show the sub-clusters of macrophages (Mφ) in aortic arches between
934 WT (left) and *Saa3*$^{-/-}$ (right) mice. Macrophages are delineated based on their gene
935 expression profiles: CD74^{hi}MHCII^{hi} Mφ in navy blue, Folr2^{hi} Mφ in red,
936 Retnla^{hi}Ear2^{hi} Mφ in green, Trem2^{hi} Mφ in sky blue, and Apbb2^{hi} Mφ in pink.
937 **(b)** The bar graph displays the percentage composition of various macrophage
938 subpopulations within total macrophages from WT and *Saa3*$^{-/-}$ mice. Different colors
939 represent distinct macrophage subpopulations as indicated in **(a)**.
940 **(c)** Dot plot representing the expression profiles of five sub-macrophage populations.
941 The x-axis lists genes with differential expression, while the y-axis indicates the sub-
942 macrophage clusters.
943 **(d)** Dot plots show the expression profiles of macrophage markers involved in
944 pathways of chemokine, IFN (interferon), inflammatory, and type II responses across

945 sub-macrophage clusters. For **(c)** and **(d)**, the size of each dot corresponds to the
946 percentage of the indicated cell cluster expressing a particular gene marker, and the
947 color intensity signifies the mean expression level within that cell cluster.
948 **(e)** Bar plots show the number (left) and strength (right) of inferred intercellular
949 communication networks in total aortic macrophages from WT and *Saa3*$^{-/-}$ mice.
950 **(f)** Heatmap visualization of overall signaling patterns in aortic macrophages of WT
951 and *Saa3*$^{-/-}$ mice. The top-colored bar plot represents the sum of each column of
952 values (signaling the strength of overall pathways) across sub-clusters. The gradient
953 blue colored bar represents the relative strength of the indicated pathway.
954 **(g)** The bar graph displays the relative information flow of various signaling
955 molecules in aortic macrophages of WT and *Saa3*$^{-/-}$ mice. Blue bars indicate higher
956 relative information flow in WT macrophages, while red bars indicate higher
957 information flow in *Saa3*$^{-/-}$ macrophages.
958
959 **Fig. 4 *Saa3* deficient impacts gene expression profiles of aortic macrophages**
960 **(a)-(d)** Volcano plot illustrating differential gene expression in four sub-macrophage
961 populations (CD74^{hi} MHCII^{hi} , Folr2^{hi}, Retnla^{hi} Ear2^{hi}, and Apbb2^{hi} macrophage(Mφ))
962 within aortic arches of WT versus *Saa3*$^{-/-}$ mice. The x-axis displays the $\log_2$ fold
963 change, while the y-axis shows the -Log_{10} p-value. Grey dots denote genes without
964 significant differences, green dots indicate genes with significant fold changes, and
965 red dots mark genes significant in both fold change and *p*-value. The dashed vertical
966 lines represent the fold change boundaries, and the dashed horizontal line
967 demonstrates the *p*-value significance threshold.
968 **(e)-(h)** The bubble plot presents the GO enrichment analysis for CD74^{hi} MHCII^{hi} ,
969 Folr2^{hi}, Retnla^{hi} Ear2^{hi}, and Apbb2^{hi} aortic macrophage (Mφ) from WT and *Saa3*$^{-/-}$

970 mice. The x-axis represents the GeneRatio. The y-axis lists the enriched GO terms.
971 Bubble size corresponds to the count of DEGs associated with each GO term. The
972 color gradient from blue to red represents the -$\log_{10}$ (adjusted *p*-value) of the
973 enrichment.
974
975 **Fig. 5 Aortic Trem2^{hi} macrophages in *Saa3*$^{-/-}$ mice express more lipid metabolism**
976 **and tissue repair-associated genes.**
977 **(a)** Volcano plot illustrating differential gene expression in aortic Trem2^{hi}
978 macrophage (Mφ) population of *Saa3*$^{-/-}$ versus WT mice.
979 **(b)** The bubble plot presents the GO enrichment analysis for Trem2^{hi} Mφ from WT
980 versus *Saa3*$^{-/-}$ (upper panel) or *Saa3*$^{-/-}$ versus WT (lower panel) mice.
981 **(c)** Violin plots depicting the expression levels of tissue repair-associated genes in
982 Trem2^{hi} Mφ from WT and *Saa3*$^{-/-}$ mice aortas. Each plot indicates the gene expression
983 level for *Gpnmb*, *Fabp5*, *Lpl*, *Lgals3*, *Spp1*, *Cd36*, and *Pparg*, with blue representing
984 WT and red for *Saa3*$^{-/-}$ group. The central white bar denotes the median expression
985 level, while the thick bar within the violins indicates the interquartile range. The
986 width of the violins reflects the density of data points at different expression levels.
987 **(d)** The circular diagram illustrates the GDF signaling pathway networks in aortic
988 macrophage subpopulations from WT (left) and *Saa3*$^{-/-}$ (right) mice. Each segment of
989 the circle represents a different macrophage subpopulation. The connections between
990 segments indicate interactions and signaling pathways shared among these
991 subpopulations.
992 **(e)** Heatmap representation of the inferred GDF signaling pathway network across
993 five sub-populations of aortic macrophages. Each column represents a specific

macrophage sub-population, while each row corresponds to the role of the population in the signaling pathway as a sender, receiver, mediator, or influencer.

Fig. 6 SAA3 modulates cholesterol metabolism, inflammatory gene expression, and immune response pathways in macrophages under steady-state condition or during foamy macrophage differentiation.

(a) Schematic overview of the experimental design. Bone marrow cells were isolated from WT and *Saa3*$^{-/-}$ mice. Then cultured and differentiated into bone marrow-derived macrophages (BMDMs), followed by treatment with soluble cholesterol to induce foamy macrophages or recombinant SAA3 protein. Downstream analyses included real-time PCR and single-cell RNA sequencing (scRNA-seq) using Parse Evercode™.

(b-c) As treatment conditions in **(a)**, Real-time PCR analysis of genes involved in inflammatory cytokines (*Il1b*, *Tnf*) and cholesterol metabolism (*Abca1*, *Abcg1*, *Cyp51*, *Hmgcr*) and under various treatment conditions. Data are represented as relative gene expression normalized to the control group, with significant differences marked by asterisks (*$p < 0.05$, **$p < 0.01$, ***$p < 0.001$). The symbols represent the following comparisons: **φ** indicates SAA3-treated male WT BMDMs versus male WT BMDMs cultured in media alone, **§** indicates SAA3-treated female WT BMDMs versus female WT BMDMs cultured in media alone, **#** indicates SAA3-treated male WT BMDMs in the presence of soluble cholesterol versus male WT BMDMs in soluble cholesterol media alone, and **†** indicates SAA3-treated female WT BMDMs in the presence of soluble cholesterol versus female WT BMDMs in soluble cholesterol media alone. The number of symbols denotes the level of statistical significance,

1018 where one symbol indicates $p < 0.05$, two symbols indicate $p < 0.01$, and three
1019 symbols indicate $p < 0.001$.
1020 **(d-f)** scRNA-seq analysis of WT BMDMs treated with media alone or SAA3 protein.
1021 **(d-e)** Dot plots show average expression (color intensity) and the percentage of cells
1022 expressing key genes (dot size) related to tissue repair, lipid metabolism, and
1023 inflammatory pathways.
1024 **(f)** Gene Ontology (GO) enrichment analysis of pathways upregulated in SAA3-
1025 treated BMDMs compared to controls. The size of the dots represents the gene ratio,
1026 and color intensity represents statistical significance ($-\log_{10}$ (adjusted *p*-value)).
1027 Statistical significance was determined using ANOVA or t-tests where appropriate.
1028

1029 ## Supplementary Figure Legends

1030

1031 **Supplementary Fig. 1 Sorting strategy of aortic CD45+ cells.**
1032 Flow cytometry analysis was performed for cell sorting to isolate CD45+ immune
1033 cells from aortic arches stained for CD45 Alexa 488 and Live/Dead Blue. The top left
1034 plot shows forward scatter (FSC-A) versus side scatter (SSC-A), differentiating cells
1035 based on size and granularity, with a population gated as P1. The top right plot
1036 presents FSC-A versus FSC-H, with the discrimination gate P2 to exclude cell
1037 aggregates. The bottom left plot displays SSC-A against the Live/Dead Blue, with live
1038 cells gated as P7. The bottom right plot demonstrates SSC-A against the fluorescence
1039 intensity of CD45 Alexa-488, with the CD45+ population gated as P8. The CD45+
1040 cells were sorted from P8 gated population.
1041
1042
1043 **Supplementary Fig. 2 Heatmap of top 10 gene markers and GO enrichment**
1044 **analysis of five aortic macrophage sub-cluster.**

1045 **(a)** Heatmap of top 10 marker genes of each sub-macrophage population in aortic
1046 arches from WT and *Saa3*$^{-/-}$ mice. The selection of these top marker genes was based
1047 on the results of a Wilcoxon test for differential expression.
1048 **(b)** Gene Ontology (GO) enrichment analysis of biological pathways in 5 sub-
1049 populations of aortic macrophage (Mφ), using differentially expressed genes (DEGs)
1050 identified when comparing one of specific Mφ sub-population against the rest of all
1051 other Mφ sub-populations. It can represent the functional characteristics of each Mφ
1052 sub-population.
1053
1054 **Supplementary Fig. 3 Comparison of ligand-receptor pair differences across five**
1055 **sub-macrophage populations between WT and *Saa3*$^{-/-}$ mice.**
1056 The bubble plot illustrating the protein-protein interaction probabilities between
1057 various ligand-receptor pairs across **(a)** CD74^{hi} MHCII^{hi} macrophage (Mφ), **(b)**
1058 Folr2^{hi} Mφ, **(c)** Retnla^{hi} Ear2^{hi} Mφ, **(d)** Trem2^{hi} Mφ, and **(e)** Apbb2^{hi} Mφ between WT
1059 and *Saa3*$^{-/-}$ mice. The x-axis categorizes the conditions under which the interactions
1060 were assessed. The y-axis lists the ligand-receptor pairs. Each bubble's color
1061 corresponds to the communication probability, with a gradient from minimum (blue)
1062 to maximum (red). The communication probability can be seen as a numerical value
1063 representing how strong or likely this interaction is between specific cell types. The
1064 size of each bubble represents the *p*-value of the interaction.
1065
1066 **Supplementary Fig. 4 Comparison of differences in the expression level of**
1067 **cholesterol efflux and lipid metabolism genes from Trem2^{hi} macrophages**
1068 **between WT and *Saa3*$^{-/-}$ mice.**
1069 Differential gene expression in aortic Trem2^{hi} macrophages (Mφ) from WT and *Saa3*$^{-}$
1070 $^{/-}$ mice. Violin plots illustrate the distribution of expression levels for genes involved
1071 in cholesterol efflux and lipid metabolism in Trem2^{hi} macrophages. Blue represents
1072 WT macrophages, while red indicates *Saa3*$^{-/-}$ macrophages.
1073
1074

1075 **References**

1076 1. Benjamin EJ, Muntner P, Alonso A, Bittencourt MS, Callaway CW, Carson AP, et
1077 al. Heart Disease and Stroke Statistics-2019 Update: A Report From the American Heart
1078 Association. Circulation. 2019;139(10):e56-e528. doi:
1079 10.1161/CIR.0000000000000659. PubMed PMID: 30700139.

1080 2. Malekmohammad K, Bezsonov EE, Rafieian-Kopaei M. Role of Lipid
1081 Accumulation and Inflammation in Atherosclerosis: Focus on Molecular and Cellular
1082 Mechanisms. Front Cardiovasc Med. 2021;8:707529. Epub 20210906. doi:
1083 10.3389/fcvm.2021.707529. PubMed PMID: 34552965; PubMed Central PMCID:
1084 PMCPMC8450356.

1085 3. Libby P, Buring JE, Badimon L, Hansson GK, Deanfield J, Bittencourt MS, et al.
1086 Atherosclerosis. Nat Rev Dis Primers. 2019;5(1):56. Epub 20190816. doi:
1087 10.1038/s41572-019-0106-z. PubMed PMID: 31420554.

1088 4. Steinl DC, Kaufmann BA. Ultrasound imaging for risk assessment in
1089 atherosclerosis. Int J Mol Sci. 2015;16(5):9749-69. Epub 20150429. doi:
1090 10.3390/ijms16059749. PubMed PMID: 25938969; PubMed Central PMCID:
1091 PMCPMC4463615.

1092 5. Sekalska B. [Aortic expression of monocyte chemotactic protein-1 (MCP-1) gene
1093 in rabbits with experimental atherosclerosis]. Ann Acad Med Stetin. 2003;49:79-90.
1094 PubMed PMID: 15552841.

1095 6. Zhang Y, Dong D, Xu X, He H, Zhu Y, Lei T, et al. Oxidized high-density
1096 lipoprotein promotes CD36 palmitoylation and increases lipid uptake in macrophages.
1097 J Biol Chem. 2022;298(6):102000. Epub 20220429. doi: 10.1016/j.jbc.2022.102000.
1098 PubMed PMID: 35500650; PubMed Central PMCID: PMCPMC9144050.

1099 7. Javadifar A, Rastgoo S, Banach M, Jamialahmadi T, Johnston TP, Sahebkar A.
1100 Foam Cells as Therapeutic Targets in Atherosclerosis with a Focus on the Regulatory
1101 Roles of Non-Coding RNAs. Int J Mol Sci. 2021;22(5). Epub 20210303. doi:
1102 10.3390/ijms22052529. PubMed PMID: 33802600; PubMed Central PMCID:
1103 PMCPMC7961492.

1104 8. Lin JD, Nishi H, Poles J, Niu X, McCauley C, Rahman K, et al. Single-cell
1105 analysis of fate-mapped macrophages reveals heterogeneity, including stem-like
1106 properties, during atherosclerosis progression and regression. JCI Insight. 2019;4(4).
1107 Epub 20190221. doi: 10.1172/jci.insight.124574. PubMed PMID: 30830865; PubMed
1108 Central PMCID: PMCPMC6478411.

9. Zhang K, Wang Y, Chen S, Mao J, Jin Y, Ye H, et al. TREM2(hi) resident macrophages protect the septic heart by maintaining cardiomyocyte homeostasis. Nat Metab. 2023;5(1):129-46. Epub 20230112. doi: 10.1038/s42255-022-00715-5. PubMed PMID: 36635449; PubMed Central PMCID: PMCPMC9886554.

10. Jung SH, Hwang BH, Shin S, Park EH, Park SH, Kim CW, et al. Spatiotemporal dynamics of macrophage heterogeneity and a potential function of Trem2(hi) macrophages in infarcted hearts. Nat Commun. 2022;13(1):4580. Epub 20220806. doi: 10.1038/s41467-022-32284-2. PubMed PMID: 35933399; PubMed Central PMCID: PMCPMC9357004.

11. den Hartigh LJ, May KS, Zhang XS, Chait A, Blaser MJ. Serum amyloid A and metabolic disease: evidence for a critical role in chronic inflammatory conditions. Front Cardiovasc Med. 2023;10:1197432. Epub 20230615. doi: 10.3389/fcvm.2023.1197432. PubMed PMID: 37396595; PubMed Central PMCID: PMCPMC10311072.

12. Reigstad CS, Lunden GO, Felin J, Backhed F. Regulation of serum amyloid A3 (SAA3) in mouse colonic epithelium and adipose tissue by the intestinal microbiota. PLoS One. 2009;4(6):e5842. Epub 20090609. doi: 10.1371/journal.pone.0005842. PubMed PMID: 19513118; PubMed Central PMCID: PMCPMC2688757.

13. Smit V, de Mol J, Kleijn M, Depuydt MAC, de Winther MPJ, Bot I, et al. Sexual dimorphism in atherosclerotic plaques of aged Ldlr(-/-) mice. Immun Ageing. 2024;21(1):27. Epub 20240502. doi: 10.1186/s12979-024-00434-3. PubMed PMID: 38698438; PubMed Central PMCID: PMCPMC11064395.

14. Chait A, Wang S, Goodspeed L, Gomes D, Turk KE, Wietecha T, et al. Sexually Dimorphic Relationships Among Saa3 (Serum Amyloid A3), Inflammation, and Cholesterol Metabolism Modulate Atherosclerosis in Mice. Arterioscler Thromb Vasc Biol. 2021;41(6):e299-e313. Epub 20210325. doi: 10.1161/ATVBAHA.121.316066. PubMed PMID: 33761762; PubMed Central PMCID: PMCPMC8159856.

15. Reigstad CS, Backhed F. Microbial regulation of SAA3 expression in mouse colon and adipose tissue. Gut Microbes. 2010;1(1):55-7. doi: 10.4161/gmic.1.1.10514. PubMed PMID: 21327118; PubMed Central PMCID: PMCPMC3035134.

16. Dong Z, Wu T, Qin W, An C, Wang Z, Zhang M, et al. Serum amyloid A directly accelerates the progression of atherosclerosis in apolipoprotein E-deficient mice. Mol Med. 2011;17(11-12):1357-64. Epub 20110921. doi: 10.2119/molmed.2011.00186. PubMed PMID: 21953420; PubMed Central PMCID: PMCPMC3321823.

17. Meek RL, Eriksen N, Benditt EP. Murine serum amyloid A3 is a high density apolipoprotein and is secreted by macrophages. Proc Natl Acad Sci U S A.

1992;89(17):7949-52. doi: 10.1073/pnas.89.17.7949. PubMed PMID: 1518819; PubMed Central PMCID: PMCPMC49832.

18. Sanada Y, Yamamoto T, Satake R, Yamashita A, Kanai S, Kato N, et al. Serum Amyloid A3 Gene Expression in Adipocytes is an Indicator of the Interaction with Macrophages. Sci Rep. 2016;6:38697. Epub 20161208. doi: 10.1038/srep38697. PubMed PMID: 27929048; PubMed Central PMCID: PMCPMC5144138.

19. Hadrup N, Zhernovkov V, Jacobsen NR, Voss C, Strunz M, Ansari M, et al. Acute Phase Response as a Biological Mechanism-of-Action of (Nano)particle-Induced Cardiovascular Disease. Small. 2020;16(21):e1907476. Epub 20200329. doi: 10.1002/smll.201907476. PubMed PMID: 32227434.

20. Thompson JC, Wilson PG, Shridas P, Ji A, de Beer M, de Beer FC, et al. Serum amyloid A3 is pro-atherogenic. Atherosclerosis. 2018;268:32-5. Epub 20171117. doi: 10.1016/j.atherosclerosis.2017.11.011. PubMed PMID: 29175652; PubMed Central PMCID: PMCPMC5839639.

21. Keeter WC, Carter NM, Nadler JL, Galkina EV. The AAV-PCSK9 murine model of atherosclerosis and metabolic dysfunction. Eur Heart J Open. 2022;2(3):oeac028. Epub 20220420. doi: 10.1093/ehjopen/oeac028. PubMed PMID: 35919346; PubMed Central PMCID: PMCPMC9242032.

22. Peled M, Nishi H, Weinstock A, Barrett TJ, Zhou F, Quezada A, et al. A wild-type mouse-based model for the regression of inflammation in atherosclerosis. PLoS One. 2017;12(3):e0173975. Epub 20170314. doi: 10.1371/journal.pone.0173975. PubMed PMID: 28291840; PubMed Central PMCID: PMCPMC5349694.

23. Han CY, Kang I, Omer M, Wang S, Wietecha T, Wight TN, et al. Serum amyloid A-containing HDL binds adipocyte-derived versican and macrophage-derived biglycan, reducing its antiinflammatory properties. JCI Insight. 2020;5(20). Epub 20200924. doi: 10.1172/jci.insight.142635. PubMed PMID: 32970631; PubMed Central PMCID: PMCPMC7605543.

24. Holmes N. CD45: all is not yet crystal clear. Immunology. 2006;117(2):145-55. doi: 10.1111/j.1365-2567.2005.02265.x. PubMed PMID: 16423050; PubMed Central PMCID: PMCPMC1782222.

25. Haudek SB, Xia Y, Huebener P, Lee JM, Carlson S, Crawford JR, et al. Bone marrow-derived fibroblast precursors mediate ischemic cardiomyopathy in mice. Proc Natl Acad Sci U S A. 2006;103(48):18284-9. Epub 20061117. doi: 10.1073/pnas.0608799103. PubMed PMID: 17114286; PubMed Central PMCID: PMCPMC1643845.

1179 26. Stuart T, Butler A, Hoffman P, Hafemeister C, Papalexi E, Mauck WM, 3rd, et al.
1180 Comprehensive Integration of Single-Cell Data. Cell. 2019;177(7):1888-902 e21. Epub
1181 20190606. doi: 10.1016/j.cell.2019.05.031. PubMed PMID: 31178118; PubMed
1182 Central PMCID: PMCPMC6687398.

1183 27. Aran D, Looney AP, Liu L, Wu E, Fong V, Hsu A, et al. Reference-based analysis
1184 of lung single-cell sequencing reveals a transitional profibrotic macrophage. Nat
1185 Immunol. 2019;20(2):163-72. Epub 20190114. doi: 10.1038/s41590-018-0276-y.
1186 PubMed PMID: 30643263; PubMed Central PMCID: PMCPMC6340744.

1187 28. Xu B, Chen L, Zhan Y, Marquez KNS, Zhuo L, Qi S, et al. The Biological
1188 Functions and Regulatory Mechanisms of Fatty Acid Binding Protein 5 in Various
1189 Diseases. Front Cell Dev Biol. 2022;10:857919. Epub 20220404. doi:
1190 10.3389/fcell.2022.857919. PubMed PMID: 35445019; PubMed Central PMCID:
1191 PMCPMC9013884.

1192 29. Nickl B, Qadri F, Bader M. Anti-inflammatory role of Gpnmb in adipose tissue of
1193 mice. Sci Rep. 2021;11(1):19614. Epub 20211004. doi: 10.1038/s41598-021-99090-6.
1194 PubMed PMID: 34608215; PubMed Central PMCID: PMCPMC8490452.

1195 30. Ding C, Xiao T, Deng Y, Yang H, Xu B, Li J, et al. The Teleost CXCL13-CXCR5
1196 Axis Induces Inflammatory Cytokine Expression through the Akt-NF-kappaB, p38-AP-
1197 1, and p38-NF-kappaB Pathways. J Immunol. 2024;212(2):317-34. doi:
1198 10.4049/jimmunol.2300237. PubMed PMID: 38054894.

1199 31. Han JH, Suh CH, Jung JY, Nam JY, Kwon JE, Yim H, et al. Association of
1200 CXCL10 and CXCL13 levels with disease activity and cutaneous manifestation in
1201 active adult-onset Still's disease. Arthritis Res Ther. 2015;17(1):260. Epub 20150919.
1202 doi: 10.1186/s13075-015-0773-4. PubMed PMID: 26385705; PubMed Central PMCID:
1203 PMCPMC4575437.

1204 32. Kiss MG, Papac-Milicevic N, Porsch F, Tsiantoulas D, Hendrikx T, Takaoka M, et
1205 al. Cell-autonomous regulation of complement C3 by factor H limits macrophage
1206 efferocytosis and exacerbates atherosclerosis. Immunity. 2023;56(8):1809-24 e10.
1207 Epub 20230726. doi: 10.1016/j.immuni.2023.06.026. PubMed PMID: 37499656;
1208 PubMed Central PMCID: PMCPMC10529786.

1209 33. Suzuki M, Becker L, Pritchard DK, Gharib SA, Wijsman EM, Bammler TK, et al.
1210 Cholesterol accumulation regulates expression of macrophage proteins implicated in
1211 proteolysis and complement activation. Arterioscler Thromb Vasc Biol.
1212 2012;32(12):2910-8. Epub 20121004. doi: 10.1161/ATVBAHA.112.300383. PubMed
1213 PMID: 23042816; PubMed Central PMCID: PMCPMC3501207.

1214 34. Wu T, Hu E, Xu S, Chen M, Guo P, Dai Z, et al. clusterProfiler 4.0: A universal
1215 enrichment tool for interpreting omics data. Innovation (Camb). 2021;2(3):100141.
1216 Epub 20210701. doi: 10.1016/j.xinn.2021.100141. PubMed PMID: 34557778;
1217 PubMed Central PMCID: PMCPMC8454663.

1218 35. Hou P, Fang J, Liu Z, Shi Y, Agostini M, Bernassola F, et al. Macrophage
1219 polarization and metabolism in atherosclerosis. Cell Death Dis. 2023;14(10):691. Epub
1220 20231020. doi: 10.1038/s41419-023-06206-z. PubMed PMID: 37863894; PubMed
1221 Central PMCID: PMCPMC10589261.

1222 36. Cochain C, Vafadarnejad E, Arampatzi P, Pelisek J, Winkels H, Ley K, et al.
1223 Single-Cell RNA-Seq Reveals the Transcriptional Landscape and Heterogeneity of
1224 Aortic Macrophages in Murine Atherosclerosis. Circ Res. 2018;122(12):1661-74. Epub
1225 20180315. doi: 10.1161/CIRCRESAHA.117.312509. PubMed PMID: 29545365.

1226 37. Nalio Ramos R, Missolo-Koussou Y, Gerber-Ferder Y, Bromley CP, Bugatti M,
1227 Nunez NG, et al. Tissue-resident FOLR2(+) macrophages associate with CD8(+) T cell
1228 infiltration in human breast cancer. Cell. 2022;185(7):1189-207 e25. Epub 20220323.
1229 doi: 10.1016/j.cell.2022.02.021. PubMed PMID: 35325594.

1230 38. Ensan S, Li A, Besla R, Degousee N, Cosme J, Roufaiel M, et al. Self-renewing
1231 resident arterial macrophages arise from embryonic CX3CR1(+) precursors and
1232 circulating monocytes immediately after birth. Nat Immunol. 2016;17(2):159-68. Epub
1233 20151207. doi: 10.1038/ni.3343. PubMed PMID: 26642357.

1234 39. Beckers CML, Simpson KR, Griffin KJ, Brown JM, Cheah LT, Smith KA, et al.
1235 Cre/lox Studies Identify Resident Macrophages as the Major Source of Circulating
1236 Coagulation Factor XIII-A. Arterioscler Thromb Vasc Biol. 2017;37(8):1494-502.
1237 Epub 20170608. doi: 10.1161/ATVBAHA.117.309271. PubMed PMID: 28596376;
1238 PubMed Central PMCID: PMCPMC5526434.

1239 40. Sanin DE, Ge Y, Marinkovic E, Kabat AM, Castoldi A, Caputa G, et al. A common
1240 framework of monocyte-derived macrophage activation. Sci Immunol.
1241 2022;7(70):eabl7482. Epub 20220415. doi: 10.1126/sciimmunol.abl7482. PubMed
1242 PMID: 35427180.

1243 41. Loke P, Lin JD. Redefining inflammatory macrophage phenotypes across stages
1244 and tissues by single-cell transcriptomics. Sci Immunol. 2022;7(70):eabo4652. Epub
1245 20220415. doi: 10.1126/sciimmunol.abo4652. PubMed PMID: 35427177.

1246 42. Cochain C, Vafadarnejad E, Arampatzi P, Jaroslav P, Winkels H, Ley K, et al.
1247 Single-Cell RNA-Seq Reveals the Transcriptional Landscape and Heterogeneity of
1248 Aortic Macrophages in Murine Atherosclerosis. Circ Res. 2018;122:1661-74. Epub

1249 2018/03/17. doi: CIRCRESAHA.117.312509 [pii]

1250 10.1161/CIRCRESAHA.117.312509. PubMed PMID: 29545365.

1251 43. Muller A, Beck K, Rancic Z, Muller C, Fischer CR, Betzel T, et al. Imaging
1252 atherosclerotic plaque inflammation via folate receptor targeting using a novel 18F-
1253 folate radiotracer. Mol Imaging. 2014;13:1-11. PubMed PMID: 24622812.

1254 44. Kim K, Shim D, Lee JS, Zaitsev K, Williams JW, Kim KW, et al. Transcriptome
1255 Analysis Reveals Nonfoamy Rather Than Foamy Plaque Macrophages Are
1256 Proinflammatory in Atherosclerotic Murine Models. Circ Res. 2018;123(10):1127-42.
1257 doi: 10.1161/CIRCRESAHA.118.312804. PubMed PMID: 30359200; PubMed Central
1258 PMCID: PMCPMC6945121.

1259 45. Qi J, Sun H, Zhang Y, Wang Z, Xun Z, Li Z, et al. Single-cell and spatial analysis
1260 reveal interaction of FAP(+) fibroblasts and SPP1(+) macrophages in colorectal cancer.
1261 Nat Commun. 2022;13(1):1742. Epub 20220401. doi: 10.1038/s41467-022-29366-6.
1262 PubMed PMID: 35365629; PubMed Central PMCID: PMCPMC8976074.

1263 46. Hoeft K, Schaefer GJL, Kim H, Schumacher D, Bleckwehl T, Long Q, et al.
1264 Platelet-instructed SPP1(+) macrophages drive myofibroblast activation in fibrosis in a
1265 CXCL4-dependent manner. Cell Rep. 2023;42(2):112131. Epub 20230218. doi:
1266 10.1016/j.celrep.2023.112131. PubMed PMID: 36807143; PubMed Central PMCID:
1267 PMCPMC9992450.

1268 47. Saade M, Araujo de Souza G, Scavone C, Kinoshita PF. The Role of GPNMB in
1269 Inflammation. Front Immunol. 2021;12:674739. Epub 20210512. doi:
1270 10.3389/fimmu.2021.674739. PubMed PMID: 34054862; PubMed Central PMCID:
1271 PMCPMC8149902.

1272 48. Kumari A, Kristensen KK, Ploug M, Winther AL. The Importance of Lipoprotein
1273 Lipase Regulation in Atherosclerosis. Biomedicines. 2021;9(7). Epub 20210706. doi:
1274 10.3390/biomedicines9070782. PubMed PMID: 34356847; PubMed Central PMCID:
1275 PMCPMC8301479.

1276 49. Wang X, Khalil RA. Matrix Metalloproteinases, Vascular Remodeling, and
1277 Vascular Disease. Adv Pharmacol. 2018;81:241-330. Epub 20170919. doi:
1278 10.1016/bs.apha.2017.08.002. PubMed PMID: 29310800; PubMed Central PMCID:
1279 PMCPMC5765875.

1280 50. Zou Y, Hu M, Lee J, Nambiar SM, Garcia V, Bao Q, et al. Nrf2 is essential for
1281 timely M phase entry of replicating hepatocytes during liver regeneration. Am J Physiol
1282 Gastrointest Liver Physiol. 2015;308(4):G262-8. Epub 20141218. doi:

1283 10.1152/ajpgi.00332.2014. PubMed PMID: 25524062; PubMed Central PMCID:
1284 PMCPMC4329475.

1285 51. Buechler C, Ritter M, Orso E, Langmann T, Klucken J, Schmitz G. Regulation of
1286 scavenger receptor CD163 expression in human monocytes and macrophages by pro-
1287 and antiinflammatory stimuli. J Leukoc Biol. 2000;67(1):97-103. PubMed PMID:
1288 10648003.

1289 52. Martinez FO, Gordon S. The M1 and M2 paradigm of macrophage activation: time
1290 for reassessment. F1000Prime Rep. 2014;6:13. Epub 20140303. doi: 10.12703/P6-13.
1291 PubMed PMID: 24669294; PubMed Central PMCID: PMCPMC3944738.

1292 53. Gudgeon J, Marin-Rubio JL, Trost M. The role of macrophage scavenger receptor
1293 1 (MSR1) in inflammatory disorders and cancer. Front Immunol. 2022;13:1012002.
1294 Epub 20221017. doi: 10.3389/fimmu.2022.1012002. PubMed PMID: 36325338;
1295 PubMed Central PMCID: PMCPMC9618966.

1296 54. Zhao SJ, Kong FQ, Jie J, Li Q, Liu H, Xu AD, et al. Macrophage MSR1 promotes
1297 BMSC osteogenic differentiation and M2-like polarization by activating
1298 PI3K/AKT/GSK3beta/beta-catenin pathway. Theranostics. 2020;10(1):17-35. Epub
1299 20200101. doi: 10.7150/thno.36930. PubMed PMID: 31903103; PubMed Central
1300 PMCID: PMCPMC6929615.

1301 55. Kurilenko N, Fatkhullina AR, Mazitova A, Koltsova EK. Act Locally, Act
1302 Globally-Microbiota, Barriers, and Cytokines in Atherosclerosis. Cells. 2021;10(2).
1303 Epub 20210207. doi: 10.3390/cells10020348. PubMed PMID: 33562334; PubMed
1304 Central PMCID: PMCPMC7915371.

1305 56. Chen HJ, Tas SW, de Winther MPJ. Type-I interferons in atherosclerosis. J Exp
1306 Med. 2020;217(1). doi: 10.1084/jem.20190459. PubMed PMID: 31821440; PubMed
1307 Central PMCID: PMCPMC7037237.

1308 57. Edsfeldt A, Swart M, Singh P, Dib L, Sun J, Cole JE, et al. Interferon regulatory
1309 factor-5-dependent CD11c+ macrophages contribute to the formation of rupture-prone
1310 atherosclerotic plaques. Eur Heart J. 2022;43(19):1864-77. Epub 20220209. doi:
1311 10.1093/eurheartj/ehab920. PubMed PMID: 35567557; PubMed Central PMCID:
1312 PMCPMC9113304.

1313 58. Stein EV, Miller TW, Ivins-O'Keefe K, Kaur S, Roberts DD. Secreted
1314 Thrombospondin-1 Regulates Macrophage Interleukin-1beta Production and
1315 Activation through CD47. Sci Rep. 2016;6:19684. Epub 20160127. doi:
1316 10.1038/srep19684. PubMed PMID: 26813769; PubMed Central PMCID:
1317 PMCPMC4728557.

1318 59. Tian Z, Miyata K, Kadomatsu T, Horiguchi H, Fukushima H, Tohyama S, et al.
1319 ANGPTL2 activity in cardiac pathologies accelerates heart failure by perturbing
1320 cardiac function and energy metabolism. Nat Commun. 2016;7:13016. Epub 20160928.
1321 doi: 10.1038/ncomms13016. PubMed PMID: 27677409; PubMed Central PMCID:
1322 PMCPMC5052800.

1323 60. Horio E, Kadomatsu T, Miyata K, Arai Y, Hosokawa K, Doi Y, et al. Role of
1324 endothelial cell-derived angptl2 in vascular inflammation leading to endothelial
1325 dysfunction and atherosclerosis progression. Arterioscler Thromb Vasc Biol.
1326 2014;34(4):790-800. Epub 20140213. doi: 10.1161/ATVBAHA.113.303116. PubMed
1327 PMID: 24526691.

1328 61. Li L, Song J, Chuquisana O, Hannocks MJ, Loismann S, Vogl T, et al. Endothelial
1329 Basement Membrane Laminins as an Environmental Cue in Monocyte Differentiation
1330 to Macrophages. Front Immunol. 2020;11:584229. Epub 20201030. doi:
1331 10.3389/fimmu.2020.584229. PubMed PMID: 33193400; PubMed Central PMCID:
1332 PMCPMC7662115.

1333 62. Wang J, Liu H. The Roles of Junctional Adhesion Molecules (JAMs) in Cell
1334 Migration. Front Cell Dev Biol. 2022;10:843671. Epub 20220309. doi:
1335 10.3389/fcell.2022.843671. PubMed PMID: 35356274; PubMed Central PMCID:
1336 PMCPMC8959349.

1337 63. Mishra BH, Mishra PP, Raitoharju E, Marttila S, Mononen N, Sievanen H, et al.
1338 Modular genome-wide gene expression architecture shared by early traits of
1339 osteoporosis and atherosclerosis in the Young Finns Study. Sci Rep. 2021;11(1):7111.
1340 Epub 20210329. doi: 10.1038/s41598-021-86536-0. PubMed PMID: 33782480;
1341 PubMed Central PMCID: PMCPMC8007808.

1342 64. Zhang Y, Xu X, Ma J, Liu Y, Duan C, Liu Y, et al. Loss of CD226 protects
1343 apolipoprotein E-deficient mice from diet-induced atherosclerosis. Biochim Biophys
1344 Acta Mol Basis Dis. 2022;1868(9):166452. Epub 20220523. doi:
1345 10.1016/j.bbadis.2022.166452. PubMed PMID: 35618182.

1346 65. Zhang M, Yue X, Zhao X, Lu Y, Liu H, Zhang Z, et al. Macrophage-specific
1347 deletion of Notch-1 induced M2 anti-inflammatory effect in atherosclerosis via
1348 activation of the PI3K-oxidative stress axis. Aging (Albany NY). 2023;15(24):15196-
1349 212. Epub 20231226. doi: 10.18632/aging.205342. PubMed PMID: 38149979;
1350 PubMed Central PMCID: PMCPMC10781475.

1351 66. Barrett TJ. Macrophages in Atherosclerosis Regression. Arterioscler Thromb Vasc
1352 Biol. 2020;40(1):20-33. Epub 20191114. doi: 10.1161/ATVBAHA.119.312802.

1353 PubMed PMID: 31722535; PubMed Central PMCID: PMCPMC6946104.

1354 67. Scott TE, Lewis CV, Zhu M, Wang C, Samuel CS, Drummond GR, et al. IL-4 and
1355 IL-13 induce equivalent expression of traditional M2 markers and modulation of
1356 reactive oxygen species in human macrophages. Sci Rep. 2023;13(1):19589. Epub
1357 20231110. doi: 10.1038/s41598-023-46237-2. PubMed PMID: 37949903; PubMed
1358 Central PMCID: PMCPMC10638413.

1359 68. Huang G, An L, Fan M, Zhang M, Chen B, Zhu M, et al. Potential role of full-
1360 length and nonfull-length progranulin in affecting aortic valve calcification. J Mol Cell
1361 Cardiol. 2020;141:93-104. Epub 20200402. doi: 10.1016/j.yjmcc.2020.03.012.
1362 PubMed PMID: 32247641.

1363 69. Saeedi-Boroujeni A, Purrahman D, Shojaeian A, Poniatowski LA, Rafiee F,
1364 Mahmoudian-Sani MR. Progranulin (PGRN) as a regulator of inflammation and a
1365 critical factor in the immunopathogenesis of cardiovascular diseases. J Inflamm (Lond).
1366 2023;20(1):1. Epub 20230119. doi: 10.1186/s12950-023-00327-0. PubMed PMID:
1367 36658641; PubMed Central PMCID: PMCPMC9851114.

1368 70. Nguyen AD, Nguyen TA, Singh RK, Eberle D, Zhang J, Abate JP, et al.
1369 Progranulin in the hematopoietic compartment protects mice from atherosclerosis.
1370 Atherosclerosis. 2018;277:145-54. Epub 20180830. doi:
1371 10.1016/j.atherosclerosis.2018.08.042. PubMed PMID: 30212683; PubMed Central
1372 PMCID: PMCPMC6432779.

1373 71. Reifenberg K, Cheng F, Orning C, Crain J, Kupper I, Wiese E, et al.
1374 Overexpression of TGF-ss1 in macrophages reduces and stabilizes atherosclerotic
1375 plaques in ApoE-deficient mice. PLoS One. 2012;7(7):e40990. Epub 20120719. doi:
1376 10.1371/journal.pone.0040990. PubMed PMID: 22829904; PubMed Central PMCID:
1377 PMCPMC3400574.

1378 72. Park I, Goddard ME, Cole JE, Zanin N, Lyytikainen LP, Lehtimaki T, et al. C-type
1379 lectin receptor CLEC4A2 promotes tissue adaptation of macrophages and protects
1380 against atherosclerosis. Nat Commun. 2022;13(1):215. Epub 20220111. doi:
1381 10.1038/s41467-021-27862-9. PubMed PMID: 35017526; PubMed Central PMCID:
1382 PMCPMC8752790.

1383 73. Chauvin C, Radulovic K, Boulard O, Delacre M, Waldschmitt N, Regnier P, et al.
1384 Loss of NOD2 in macrophages improves colitis and tumorigenesis in a lysozyme-
1385 dependent manner. Front Immunol. 2023;14:1252979. Epub 20231009. doi:
1386 10.3389/fimmu.2023.1252979. PubMed PMID: 37876927; PubMed Central PMCID:
1387 PMCPMC10590911.

1388 74. Alam MS, Getz M, Safeukui I, Yi S, Tamez P, Shin J, et al. Genomic expression
1389 analyses reveal lysosomal, innate immunity proteins, as disease correlates in murine
1390 models of a lysosomal storage disorder. PLoS One. 2012;7(10):e48273. Epub
1391 20121019. doi: 10.1371/journal.pone.0048273. PubMed PMID: 23094108; PubMed
1392 Central PMCID: PMCPMC3477142.

1393 75. Smedbakken LM, Halvorsen B, Daissormont I, Ranheim T, Michelsen AE,
1394 Skjelland M, et al. Increased levels of the homeostatic chemokine CXCL13 in human
1395 atherosclerosis - Potential role in plaque stabilization. Atherosclerosis.
1396 2012;224(1):266-73. Epub 20120720. doi: 10.1016/j.atherosclerosis.2012.06.071.
1397 PubMed PMID: 22840692.

1398 76. Dangi A, Husain I, Jordan CZ, Yu S, Natesh N, Shen X, et al. Blocking CCL8-
1399 CCR8-Mediated Early Allograft Inflammation Improves Kidney Transplant Function.
1400 J Am Soc Nephrol. 2022;33(10):1876-90. Epub 20220816. doi:
1401 10.1681/ASN.2022020139. PubMed PMID: 35973731; PubMed Central PMCID:
1402 PMCPMC9528333.

1403 77. Luo H, Li L, Han S, Liu T. The role of monocyte/macrophage chemokines in
1404 pathogenesis of osteoarthritis: A review. Int J Immunogenet. 2024;51(3):130-42. Epub
1405 20240310. doi: 10.1111/iji.12664. PubMed PMID: 38462560.

1406 78. Ricard N, Zhang J, Zhuang ZW, Simons M. Isoform-Specific Roles of ERK1 and
1407 ERK2 in Arteriogenesis. Cells. 2019;9(1). Epub 20191221. doi: 10.3390/cells9010038.
1408 PubMed PMID: 31877781; PubMed Central PMCID: PMCPMC7017123.

1409 79. Al-Ahmadi W, Webberley TS, Joseph A, Harris F, Chan YH, Alotibi R, et al. Pro-
1410 atherogenic actions of signal transducer and activator of transcription 1 serine 727
1411 phosphorylation in LDL receptor deficient mice via modulation of plaque inflammation.
1412 FASEB J. 2021;35(10):e21892. doi: 10.1096/fj.202100571RR. PubMed PMID:
1413 34569651; PubMed Central PMCID: PMCPMC9549671.

1414 80. Jin M, Fang J, Wang JJ, Shao X, Xu SW, Liu PQ, et al. Regulation of toll-like
1415 receptor (TLR) signaling pathways in atherosclerosis: from mechanisms to targeted
1416 therapeutics. Acta Pharmacol Sin. 2023;44(12):2358-75. Epub 20230807. doi:
1417 10.1038/s41401-023-01123-5. PubMed PMID: 37550526; PubMed Central PMCID:
1418 PMCPMC10692204.

1419 81. Frank JW, Seo H, Burghardt RC, Bayless KJ, Johnson GA. ITGAV (alpha v
1420 integrins) bind SPP1 (osteopontin) to support trophoblast cell adhesion. Reproduction.
1421 2017;153(5):695-706. Epub 20170301. doi: 10.1530/REP-17-0043. PubMed PMID:
1422 28250242.

1423 82. Erikson DW, Burghardt RC, Bayless KJ, Johnson GA. Secreted phosphoprotein 1
1424 (SPP1, osteopontin) binds to integrin alpha v beta 6 on porcine trophectoderm cells and
1425 integrin alpha v beta 3 on uterine luminal epithelial cells, and promotes trophectoderm
1426 cell adhesion and migration. Biol Reprod. 2009;81(5):814-25. Epub 20090701. doi:
1427 10.1095/biolreprod.109.078600. PubMed PMID: 19571258.

1428 83. Vallejo J, Duner P, To F, Engelbertsen D, Goncalves I, Nilsson J, et al. Activation
1429 of immune responses against the basement membrane component collagen type IV does
1430 not affect the development of atherosclerosis in ApoE-deficient mice. Sci Rep.
1431 2019;9(1):5964. Epub 20190412. doi: 10.1038/s41598-019-42375-8. PubMed PMID:
1432 30979943; PubMed Central PMCID: PMCPMC6461614.

1433 84. Li M, Wang M, Wen Y, Zhang H, Zhao GN, Gao Q. Signaling pathways in
1434 macrophages: molecular mechanisms and therapeutic targets. MedComm (2020).
1435 2023;4(5):e349. Epub 20230911. doi: 10.1002/mco2.349. PubMed PMID: 37706196;
1436 PubMed Central PMCID: PMCPMC10495745.

1437 85. Ruytinx P, Proost P, Van Damme J, Struyf S. Chemokine-Induced Macrophage
1438 Polarization in Inflammatory Conditions. Front Immunol. 2018;9:1930. Epub
1439 20180907. doi: 10.3389/fimmu.2018.01930. PubMed PMID: 30245686; PubMed
1440 Central PMCID: PMCPMC6137099.

1441 86. Furuhashi M, Saitoh S, Shimamoto K, Miura T. Fatty Acid-Binding Protein 4
1442 (FABP4): Pathophysiological Insights and Potent Clinical Biomarker of Metabolic and
1443 Cardiovascular Diseases. Clin Med Insights Cardiol. 2014;8(Suppl 3):23-33. Epub
1444 20150202. doi: 10.4137/CMC.S17067. PubMed PMID: 25674026; PubMed Central
1445 PMCID: PMCPMC4315049.

1446 87. Wieczorek E, Cwiklinska A, Kuchta A, Kortas-Stempak B, Gliwinska A,
1447 Jankowski M. The Differential Effects of HDL Subpopulations on Lipoprotein Lipase
1448 (LPL)-Mediated VLDL Catabolism. Biomedicines. 2021;9(12). Epub 20211205. doi:
1449 10.3390/biomedicines9121839. PubMed PMID: 34944655; PubMed Central PMCID:
1450 PMCPMC8698418.

1451 88. Fang F, Feng T, Li J, Zhang H, Wang Q, Chen Y, et al. Cathepsin K contributed to
1452 disturbed flow-induced atherosclerosis is dependent on integrin-actin cytoskeleton-NF-
1453 kappaB pathway. Genes Dis. 2023;10(2):583-95. Epub 20220425. doi:
1454 10.1016/j.gendis.2022.03.020. PubMed PMID: 37223522; PubMed Central PMCID:
1455 PMCPMC10201601.

1456 89. Zhang H, Zhang S, Dang X, Lin L, Ren L, Song R. GPNMB plays an active role
1457 in the M1/M2 balance. Tissue Cell. 2022;74:101683. Epub 20211117. doi:

1458 10.1016/j.tice.2021.101683. PubMed PMID: 34800878.

1459 90. Wang J, Zhang X, Long M, Yuan M, Yin J, Luo W, et al. Macrophage-derived
1460 GPNMB trapped by fibrotic extracellular matrix promotes pulmonary fibrosis.
1461 Commun Biol. 2023;6(1):136. Epub 20230202. doi: 10.1038/s42003-022-04333-5.
1462 PubMed PMID: 36732560; PubMed Central PMCID: PMCPMC9893197.

1463 91. Nickl B, Qadri F, Bader M. Role of Gpnmb in atherosclerosis of female mice.
1464 Biochem Biophys Res Commun. 2022;621:20-4. Epub 20220702. doi:
1465 10.1016/j.bbrc.2022.06.082. PubMed PMID: 35809343.

1466 92. Chen P, Chen Y, Wu W, Chen L, Yang X, Zhang S. Identification and validation of
1467 four hub genes involved in the plaque deterioration of atherosclerosis. Aging (Albany
1468 NY). 2019;11(16):6469-89. Epub 20190826. doi: 10.18632/aging.102200. PubMed
1469 PMID: 31449494; PubMed Central PMCID: PMCPMC6738408.

1470 93. Huang K, Chen S, Yu LJ, Wu ZM, Chen QJ, Wang XQ, et al. Serum secreted
1471 phosphoprotein 1 level is associated with plaque vulnerability in patients with coronary
1472 artery disease. Front Immunol. 2024;15:1285813. Epub 20240215. doi:
1473 10.3389/fimmu.2024.1285813. PubMed PMID: 38426091; PubMed Central PMCID:
1474 PMCPMC10902157.

1475 94. Orecchioni M, Ghosheh Y, Pramod AB, Ley K. Macrophage Polarization:
1476 Different Gene Signatures in M1(LPS+) vs. Classically and M2(LPS-) vs. Alternatively
1477 Activated Macrophages. Front Immunol. 2019;10:1084. Epub 20190524. doi:
1478 10.3389/fimmu.2019.01084. PubMed PMID: 31178859; PubMed Central PMCID:
1479 PMCPMC6543837.

1480 95. Collison J. MMP12 makes the cut. Nat Rev Rheumatol. 2018;14(9):501. doi:
1481 10.1038/s41584-018-0056-y. PubMed PMID: 30022107.

1482 96. Dean RA, Cox JH, Bellac CL, Doucet A, Starr AE, Overall CM. Macrophage-
1483 specific metalloelastase (MMP-12) truncates and inactivates ELR+ CXC chemokines
1484 and generates CCL2, -7, -8, and -13 antagonists: potential role of the macrophage in
1485 terminating polymorphonuclear leukocyte influx. Blood. 2008;112(8):3455-64. Epub
1486 20080725. doi: 10.1182/blood-2007-12-129080. PubMed PMID: 18660381.

1487 97. Willemsen L, de Winther MP. Macrophage subsets in atherosclerosis as defined
1488 by single-cell technologies. J Pathol. 2020;250(5):705-14. Epub 20200311. doi:
1489 10.1002/path.5392. PubMed PMID: 32003464; PubMed Central PMCID:
1490 PMCPMC7217201.

1491 98. Chen Y, Zhang J, Cui W, Silverstein RL. CD36, a signaling receptor and fatty acid

1492 transporter that regulates immune cell metabolism and fate. J Exp Med. 2022;219(6).
1493 Epub 20220419. doi: 10.1084/jem.20211314. PubMed PMID: 35438721; PubMed
1494 Central PMCID: PMCPMC9022290.

1495 99. Herrmann J, Lerman LO, Mukhopadhyay D, Napoli C, Lerman A. Angiogenesis
1496 in atherogenesis. Arterioscler Thromb Vasc Biol. 2006;26(9):1948-57. Epub 20060622.
1497 doi: 10.1161/01.ATV.0000233387.90257.9b. PubMed PMID: 16794218.

1498 100. Khurana R, Simons M, Martin JF, Zachary IC. Role of angiogenesis in
1499 cardiovascular disease: a critical appraisal. Circulation. 2005;112(12):1813-24. doi:
1500 10.1161/CIRCULATIONAHA.105.535294. PubMed PMID: 16172288.

1501 101. Asrih M, Wei S, Nguyen TT, Yi HS, Ryu D, Gariani K. Overview of growth
1502 differentiation factor 15 in metabolic syndrome. J Cell Mol Med. 2023;27(9):1157-67.
1503 Epub 20230329. doi: 10.1111/jcmm.17725. PubMed PMID: 36992609; PubMed
1504 Central PMCID: PMCPMC10148061.

1505 102. Adela R, Banerjee SK. GDF-15 as a Target and Biomarker for Diabetes and
1506 Cardiovascular Diseases: A Translational Prospective. J Diabetes Res.
1507 2015;2015:490842. Epub 20150727. doi: 10.1155/2015/490842. PubMed PMID:
1508 26273671; PubMed Central PMCID: PMCPMC4530250.

1509 103. Kempf T, Eden M, Strelau J, Naguib M, Willenbockel C, Tongers J, et al. The
1510 transforming growth factor-beta superfamily member growth-differentiation factor-15
1511 protects the heart from ischemia/reperfusion injury. Circ Res. 2006;98(3):351-60. Epub
1512 20060105. doi: 10.1161/01.RES.0000202805.73038.48. PubMed PMID: 16397141.

1513 104. Preusch MR, Baeuerle M, Albrecht C, Blessing E, Bischof M, Katus HA, et al.
1514 GDF-15 protects from macrophage accumulation in a mousemodel of advanced
1515 atherosclerosis. Eur J Med Res. 2013;18(1):19. Epub 20130624. doi: 10.1186/2047-
1516 783X-18-19. PubMed PMID: 23800095; PubMed Central PMCID: PMCPMC3701574.

1517 105. Kempf T, Zarbock A, Widera C, Butz S, Stadtmann A, Rossaint J, et al. GDF-15
1518 is an inhibitor of leukocyte integrin activation required for survival after myocardial
1519 infarction in mice. Nat Med. 2011;17(5):581-8. Epub 20110424. doi: 10.1038/nm.2354.
1520 PubMed PMID: 21516086.

1521 106. Johnen H, Kuffner T, Brown DA, Wu BJ, Stocker R, Breit SN. Increased
1522 expression of the TGF-b superfamily cytokine MIC-1/GDF15 protects ApoE(-/-) mice
1523 from the development of atherosclerosis. Cardiovasc Pathol. 2012;21(6):499-505. Epub
1524 20120302. doi: 10.1016/j.carpath.2012.02.003. PubMed PMID: 22386250.

1525 107. Markle JG, Frank DN, Mortin-Toth S, Robertson CE, Feazel LM, Rolle-

Kampczyk U, et al. Sex differences in the gut microbiome drive hormone-dependent regulation of autoimmunity. Science. 2013;339(6123):1084-8. Epub 20130117. doi: 10.1126/science.1233521. PubMed PMID: 23328391.

108. Kaliannan K, Robertson RC, Murphy K, Stanton C, Kang C, Wang B, et al. Estrogen-mediated gut microbiome alterations influence sexual dimorphism in metabolic syndrome in mice. Microbiome. 2018;6(1):205. Epub 20181113. doi: 10.1186/s40168-018-0587-0. PubMed PMID: 30424806; PubMed Central PMCID: PMCPMC6234624.

109. Xiao E, He L, Wu Q, Li J, He Y, Zhao L, et al. Microbiota regulates bone marrow mesenchymal stem cell lineage differentiation and immunomodulation. Stem Cell Res Ther. 2017;8(1):213. Epub 20170929. doi: 10.1186/s13287-017-0670-7. PubMed PMID: 28962644; PubMed Central PMCID: PMCPMC5622543.

110. Zhang D, Gao X, Li H, Borger DK, Wei Q, Yang E, et al. The microbiota regulates hematopoietic stem cell fate decisions by controlling iron availability in bone marrow. Cell Stem Cell. 2022;29(2):232-47 e7. Epub 20220121. doi: 10.1016/j.stem.2021.12.009. PubMed PMID: 35065706; PubMed Central PMCID: PMCPMC8818037.

111. Jylhava J, Haarala A, Eklund C, Pertovaara M, Kahonen M, Hutri-Kahonen N, et al. Serum amyloid A is independently associated with metabolic risk factors but not with early atherosclerosis: the Cardiovascular Risk in Young Finns Study. J Intern Med. 2009;266(3):286-95. doi: 10.1111/j.1365-2796.2009.02120.x. PubMed PMID: 19702793.

112. den Hartigh LJ, Wang S, Goodspeed L, Ding Y, Averill M, Subramanian S, et al. Deletion of serum amyloid A3 improves high fat high sucrose diet-induced adipose tissue inflammation and hyperlipidemia in female mice. PLoS One. 2014;9(9):e108564. Epub 20140924. doi: 10.1371/journal.pone.0108564. PubMed PMID: 25251243; PubMed Central PMCID: PMCPMC4177399.

113. Sjoholm K, Lundgren M, Olsson M, Eriksson JW. Association of serum amyloid A levels with adipocyte size and serum levels of adipokines: differences between men and women. Cytokine. 2009;48(3):260-6. Epub 20090915. doi: 10.1016/j.cyto.2009.08.005. PubMed PMID: 19758820.

Figure 1

a

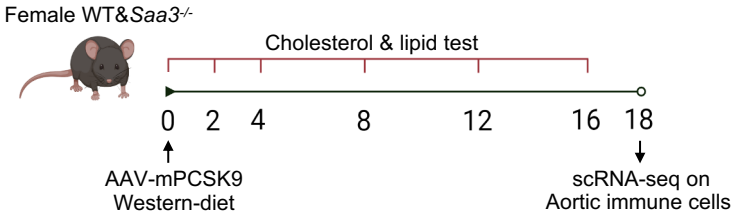

b

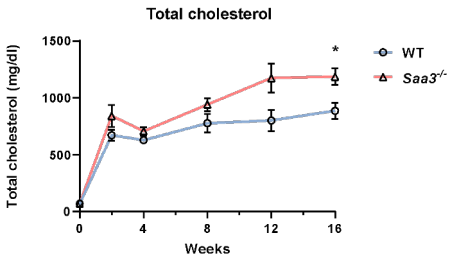

c

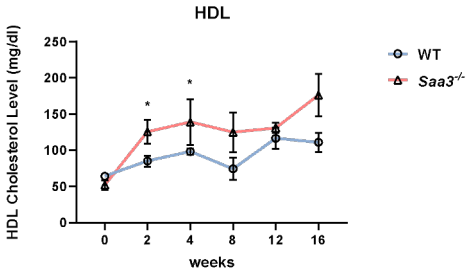

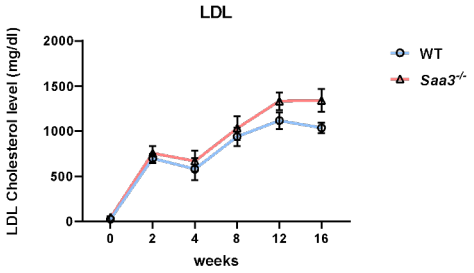

d

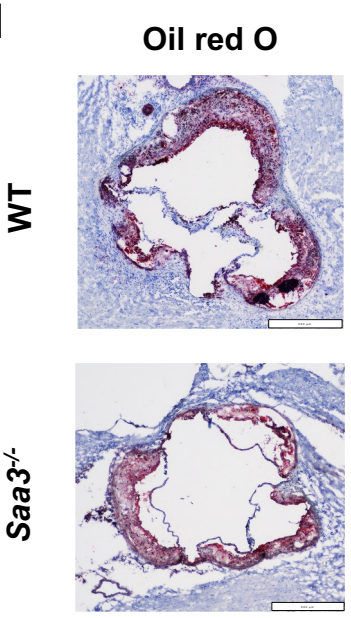

e

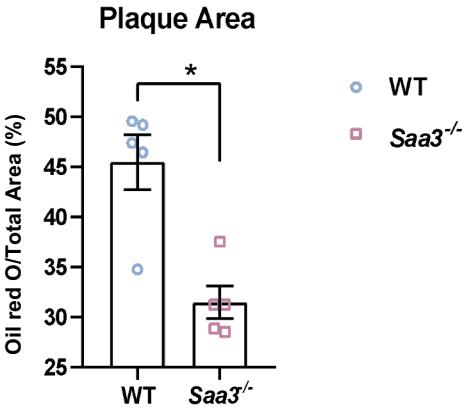

Figure 2

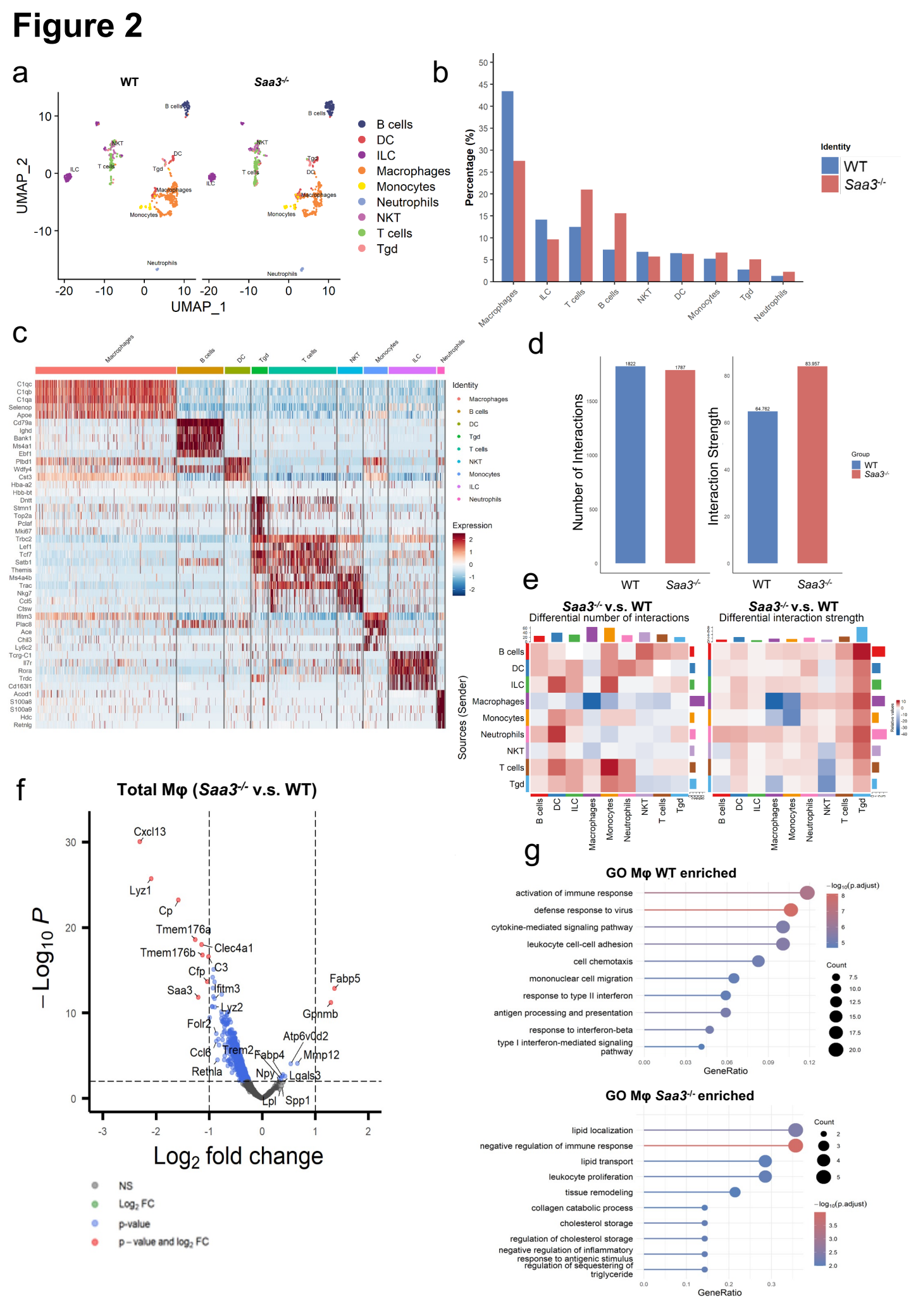
a
WT
Saa3-/-
UMAP_2
UMAP_1
B cells
DC
ILC
Macrophages
Monocytes
Neutrophils
NKT
T cells
Tgd
b
Percentage (%)
Identity
WT
Saa3-/-
c
Identity
Expression
d
Number of Interactions
Interaction Strength
Group
1822
1787
64.762
83.957
e
Saa3-/- v.s. WT
Differential number of interactions
Differential interaction strength
Sources (Sender)
f
Total Mφ (Saa3-/- v.s. WT)
Cxcl13
Lyz1
Cp
Tmem176a
Tmem176b
Clec4a1
Cfp
C3
Saa3
Ifitm3
Lyz2
Folr2
Ccl6
Trem2
Rethla
Fabp4
Npy
Lpl
Spp1
Lgals3
Mmp12
Atp6v0d2
Gpnmb
Fabp5
Log2 fold change
NS
Log2 FC
p-value
p-value and log2 FC
g
GO Mφ WT enriched
activation of immune response
defense response to virus
cytokine-mediated signaling pathway
leukocyte cell-cell adhesion
cell chemotaxis
mononuclear cell migration
response to type II interferon
antigen processing and presentation
response to interferon-beta
type I interferon-mediated signaling pathway
GeneRatio
GO Mφ Saa3-/- enriched
lipid localization
negative regulation of immune response
lipid transport
leukocyte proliferation
tissue remodeling
collagen catabolic process
cholesterol storage
regulation of cholesterol storage
negative regulation of inflammatory response to antigenic stimulus
regulation of sequestering of triglyceride
GeneRatio

Figure 3

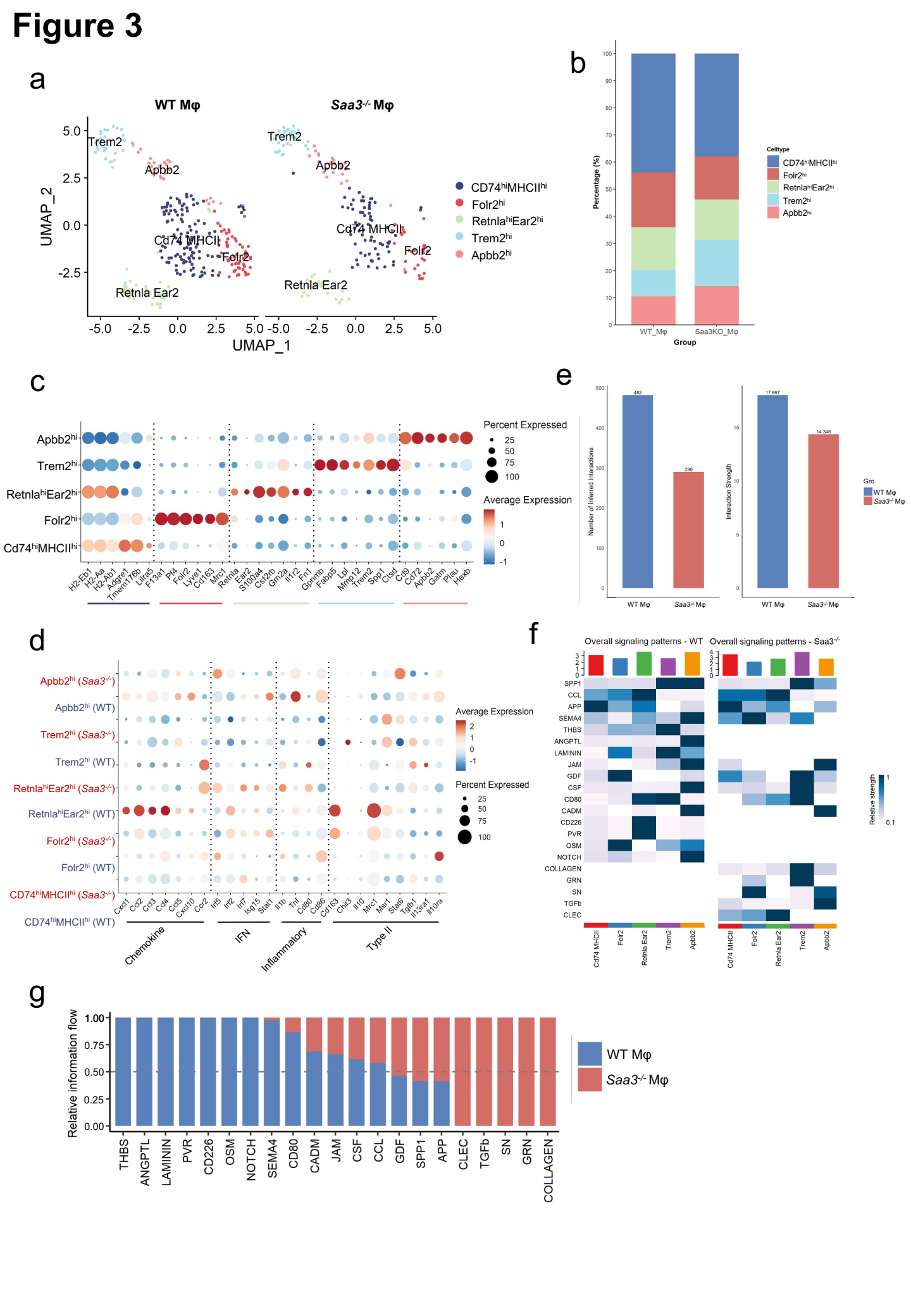
a
WT Mφ
Saa3-/- Mφ
UMAP_2
UMAP_1
Trem2
Apbb2
Cd74 MHCII
Folr2
Retnla Ear2
CD74hiMHCIIhi
Folr2hi
RetnlahiEar2hi
Trem2hi
Apbb2hi
b
Percentage (%)
Celltype
WT_Mφ
Saa3KO_Mφ
Group
c
Percent Expressed
Average Expression
H2-Eb1
H2-Aa
H2-Ab1
Adgre1
Tmem176b
Litra5
F13a1
Prf4
Folr2
Lyve1
Ccl163
Mrc1
Retnla
Ear2
S100a4
Csf2rb
Gm2a
Il1r2
Fn1
Gpnmb
Fabp5
Lpl
Mmp12
Trem2
Spp1
Ctsd
Ccl9
Ccl72
Apbb2
Gatm
Plau
Hexb
e
Number of Inferred Interactions
Interaction Strength
482
290
17.997
14.348
WT Mφ
Saa3-/- Mφ
d
Average Expression
Percent Expressed
Apbb2hi (Saa3-/-)
Apbb2hi (WT)
Trem2hi (Saa3-/-)
Trem2hi (WT)
RetnlahiEar2hi (Saa3-/-)
RetnlahiEar2hi (WT)
Folr2hi (Saa3-/-)
Folr2hi (WT)
CD74hiMHCIIhi (Saa3-/-)
CD74hiMHCIIhi (WT)
Cxcl1
Ccl2
Ccl3
Ccl4
Ccl5
Cxcl10
Ccr2
Irf5
Irf2
Irf7
Isg15
Stat1
Il1b
Tnf
Cd80
Cd86
Cd163
Chil3
Il10
Mrc1
Msr1
Stat6
Tgfb1
Il13ra1
Il10ra
Chemokine
IFN
Inflammatory
Type II
f
Overall signaling patterns - WT
Overall signaling patterns - Saa3-/-
SPP1
CCL
APP
SEMA4
THBS
ANGPTL
LAMININ
JAM
GDF
CSF
CD80
CADM
CD226
PVR
OSM
NOTCH
COLLAGEN
GRN
SN
TGFb
CLEC
Relative strength
Cd74 MHCII
Folr2
Retnla Ear2
Trem2
Apbb2
g
Relative information flow
THBS
ANGPTL
LAMININ
PVR
CD226
OSM
NOTCH
SEMA4
CD80
CADM
JAM
CSF
CCL
GDF
SPP1
APP
CLEC
TGFb
SN
GRN
COLLAGEN
WT Mφ
Saa3-/- Mφ

Figure 4

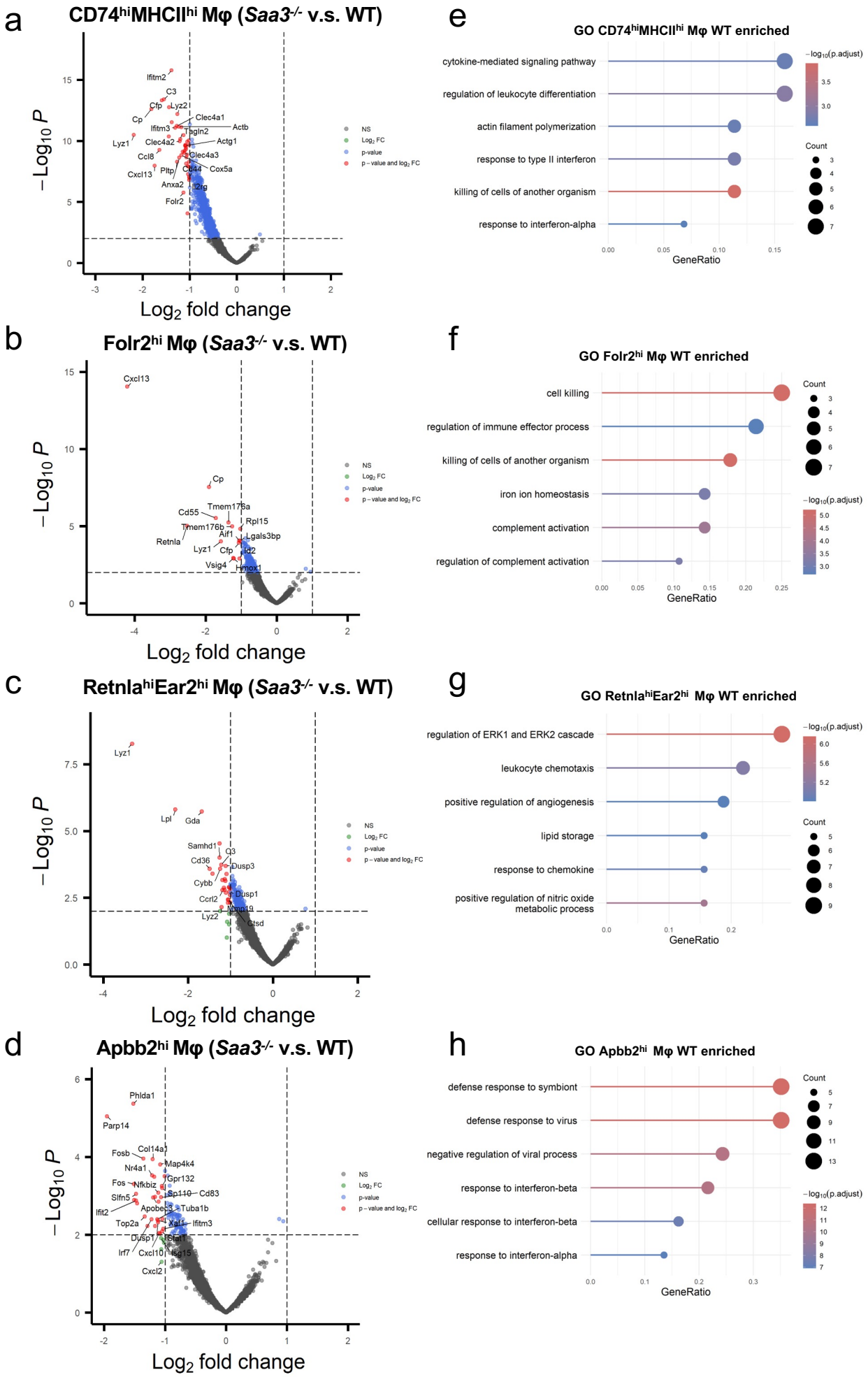
a
CD74hiMHCIIhi Mφ (Saa3-/- v.s. WT)
Ifitm2
C3
Cfp
Lyz2
Cp
Clec4a1
Ifitm3
Actb
Tagln2
Lyz1
Clec4a2
Actg1
Ccl8
Clec4a3
Cxcl13
Pltp
Ccl4
Cox5a
Anxa2
Il2rg
Folr2
NS
Log2 FC
p-value
p – value and log2 FC
– Log10 P
Log2 fold change
b
Folr2hi Mφ (Saa3-/- v.s. WT)
Cxcl13
Cp
Tmem176a
Cd55
Rpl15
Tmem176b
Aif1
Lgals3bp
Retnla
Lyz1
Cfp
Id2
Vsig4
Hmox1
c
RetnlahiEar2hi Mφ (Saa3-/- v.s. WT)
Lyz1
Lpl
Gda
Samhd1
C3
Cd36
Dusp3
Cybb
Ccrl2
Dusp1
Lyz2
Glsd
d
Apbb2hi Mφ (Saa3-/- v.s. WT)
Phlda1
Parp14
Fosb
Col14a1
Nr4a1
Map4k4
Fos
Gpr132
Nfkbiz
Slfn5
Sp110
Cd83
Ifit2
Apobec3
Tuba1b
Top2a
Xaf1
Ifitm3
Dusp1
Irf7
Cxcl10
Isg15
Cxcl2
e
GO CD74hiMHCIIhi Mφ WT enriched
cytokine-mediated signaling pathway
regulation of leukocyte differentiation
actin filament polymerization
response to type II interferon
killing of cells of another organism
response to interferon-alpha
GeneRatio
–log10(p.adjust)
Count
f
GO Folr2hi Mφ WT enriched
cell killing
regulation of immune effector process
killing of cells of another organism
iron ion homeostasis
complement activation
regulation of complement activation
GeneRatio
Count
–log10(p.adjust)
g
GO RetnlahiEar2hi Mφ WT enriched
regulation of ERK1 and ERK2 cascade
leukocyte chemotaxis
positive regulation of angiogenesis
lipid storage
response to chemokine
positive regulation of nitric oxide metabolic process
GeneRatio
–log10(p.adjust)
Count
h
GO Apbb2hi Mφ WT enriched
defense response to symbiont
defense response to virus
negative regulation of viral process
response to interferon-beta
cellular response to interferon-beta
response to interferon-alpha
GeneRatio
Count
–log10(p.adjust)

Figure 5

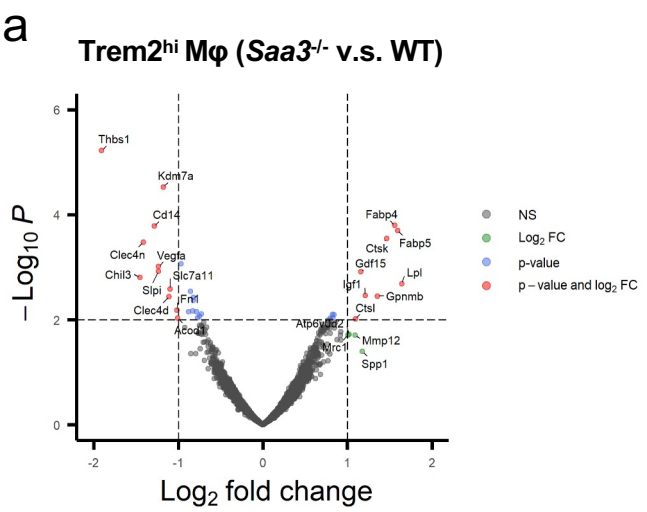
a
Trem2hi Mφ (Saa3-/- v.s. WT)
Thbs1
Kdm7a
Cd14
Clec4n
Vegfa
Chil3
Slc7a11
Slpi
Fn1
Clec4d
Acod1
Fabp4
Ctsk
Fabp5
Gdf15
Lpl
Igf1
Gpnmb
Ctsl
Atp6v0d2
Mrc1
Mmp12
Spp1
NS
Log2 FC
p-value
p – value and log2 FC
– Log10 P
Log2 fold change

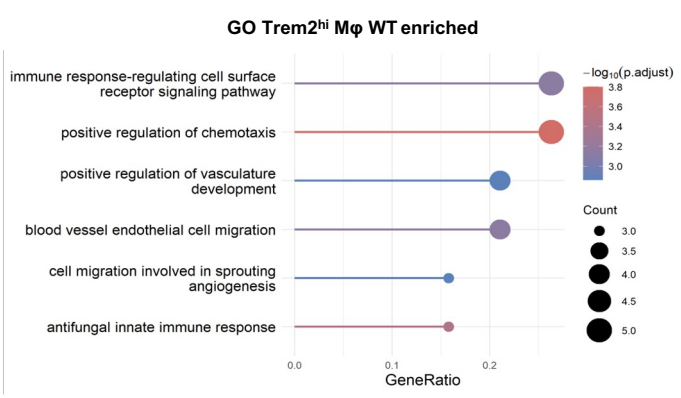
b
GO Trem2hi Mφ WT enriched
immune response-regulating cell surface receptor signaling pathway
positive regulation of chemotaxis
positive regulation of vasculature development
blood vessel endothelial cell migration
cell migration involved in sprouting angiogenesis
antifungal innate immune response
GeneRatio
–log10(p.adjust)
Count

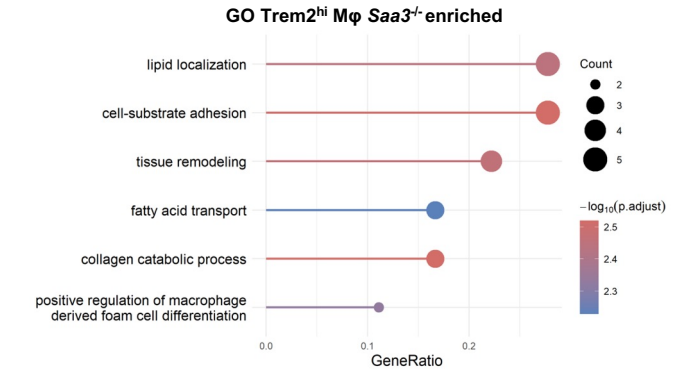
GO Trem2hi Mφ Saa3-/- enriched
lipid localization
cell-substrate adhesion
tissue remodeling
fatty acid transport
collagen catabolic process
positive regulation of macrophage derived foam cell differentiation
GeneRatio
Count
–log10(p.adjust)

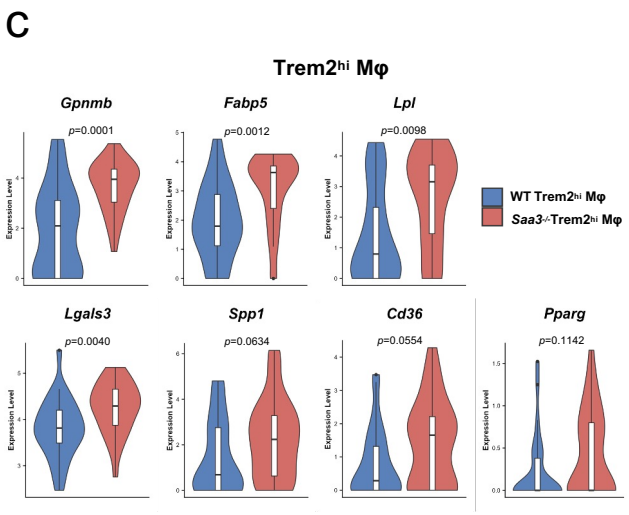
c
Trem2hi Mφ
Gpnmb
p=0.0001
Fabp5
p=0.0012
Lpl
p=0.0098
Lgals3
p=0.0040
Spp1
p=0.0634
Cd36
p=0.0554
Pparg
p=0.1142
Expression Level
WT Trem2hi Mφ
Saa3-/-Trem2hi Mφ

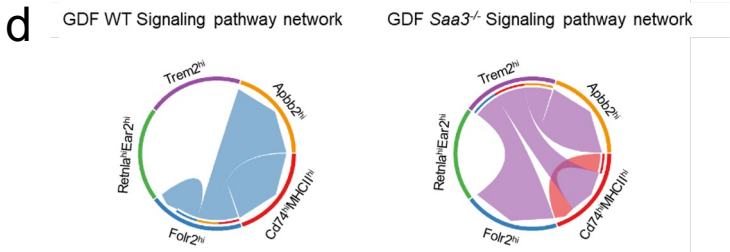
d
GDF WT Signaling pathway network
GDF Saa3-/- Signaling pathway network
Trem2hi
Apbb2hi
Cd74hiMHCIIhi
Folr2hi
Retnlahi Ear2hi

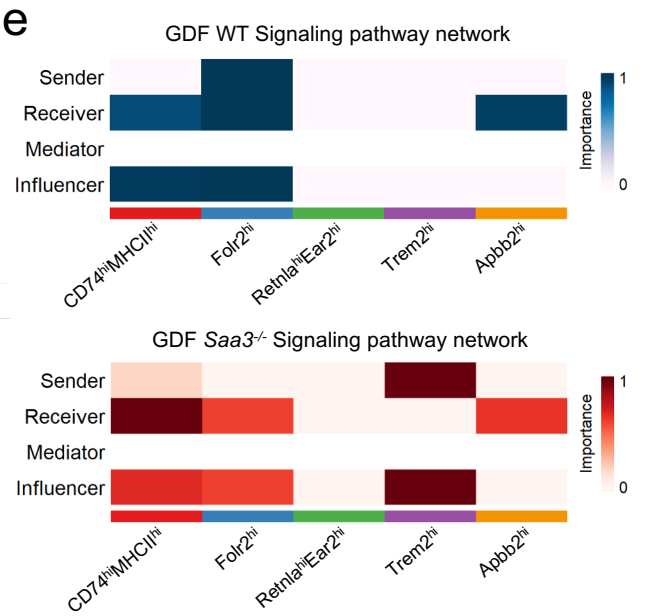
e
GDF WT Signaling pathway network
GDF Saa3-/- Signaling pathway network
Sender
Receiver
Mediator
Influencer
Importance
CD74hiMHCIIhi
Folr2hi
RetnlahiEar2hi
Trem2hi
Apbb2hi

Figure 6

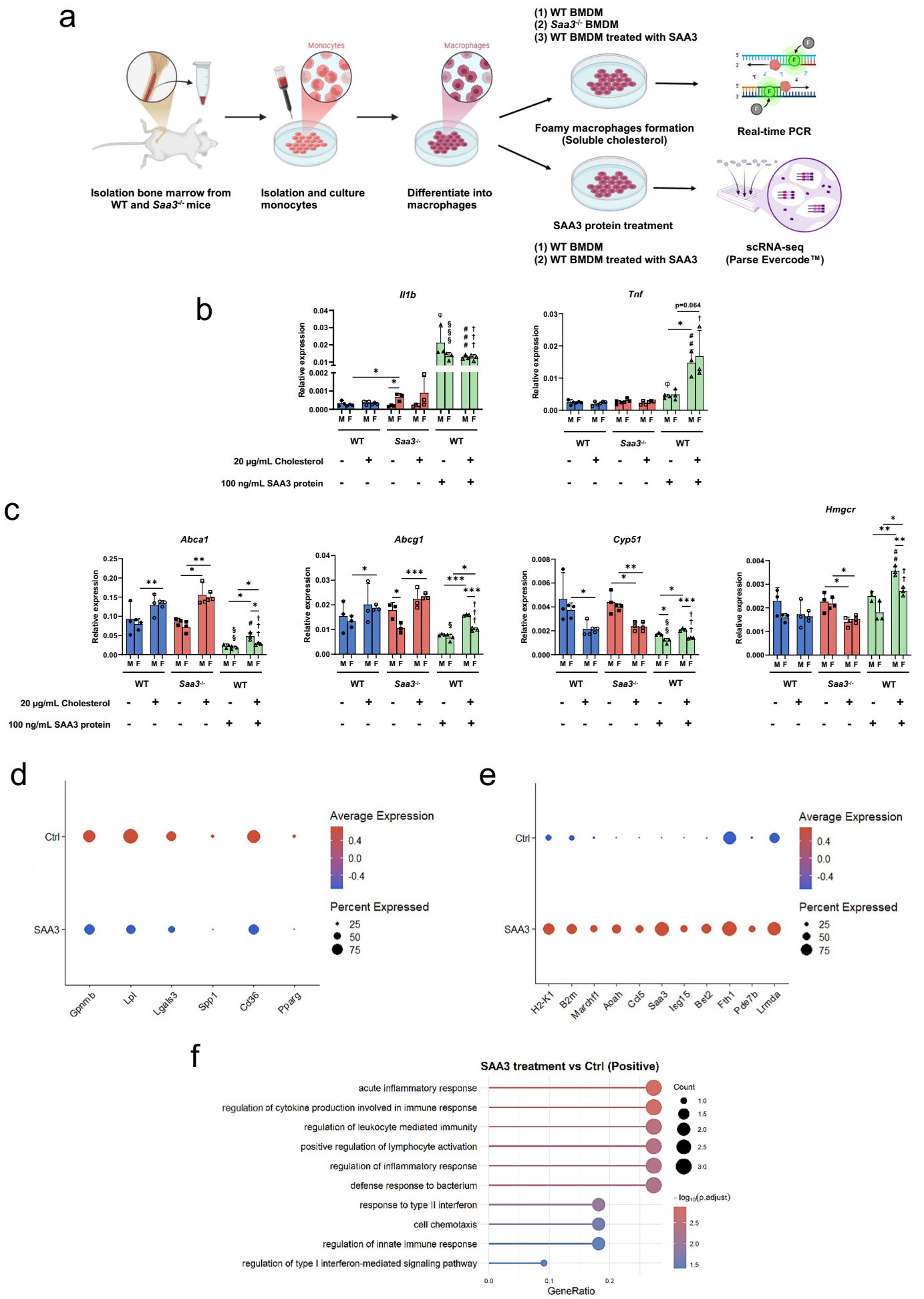
a
Monocytes
Macrophages
(1) WT BMDM
(2) Saa3-/- BMDM
(3) WT BMDM treated with SAA3
Isolation bone marrow from WT and Saa3-/- mice
Isolation and culture monocytes
Differentiate into macrophages
Foamy macrophages formation (Soluble cholesterol)
Real-time PCR
SAA3 protein treatment
(1) WT BMDM
(2) WT BMDM treated with SAA3
scRNA-seq (Parse Evercode™)
b
Il1b
Tnf
p=0.064
Relative expression
WT
Saa3-/-
20 μg/mL Cholesterol
100 ng/mL SAA3 protein
c
Abca1
Abcg1
Cyp51
Hmgcr
d
Ctrl
SAA3
Gpnmb
Lpl
Lgals3
Spp1
Cd36
Pparg
Average Expression
Percent Expressed
e
H2-K1
B2m
Marchf1
Aoah
Ccl5
Saa3
Isg15
Bst2
Fth1
Pde7b
Lrmda
f
SAA3 treatment vs Ctrl (Positive)
acute inflammatory response
regulation of cytokine production involved in immune response
regulation of leukocyte mediated immunity
positive regulation of lymphocyte activation
regulation of inflammatory response
defense response to bacterium
response to type II interferon
cell chemotaxis
regulation of innate immune response
regulation of type I interferon-mediated signaling pathway
Count
−log10(p.adjust)
GeneRatio

Supplementary Figure 1

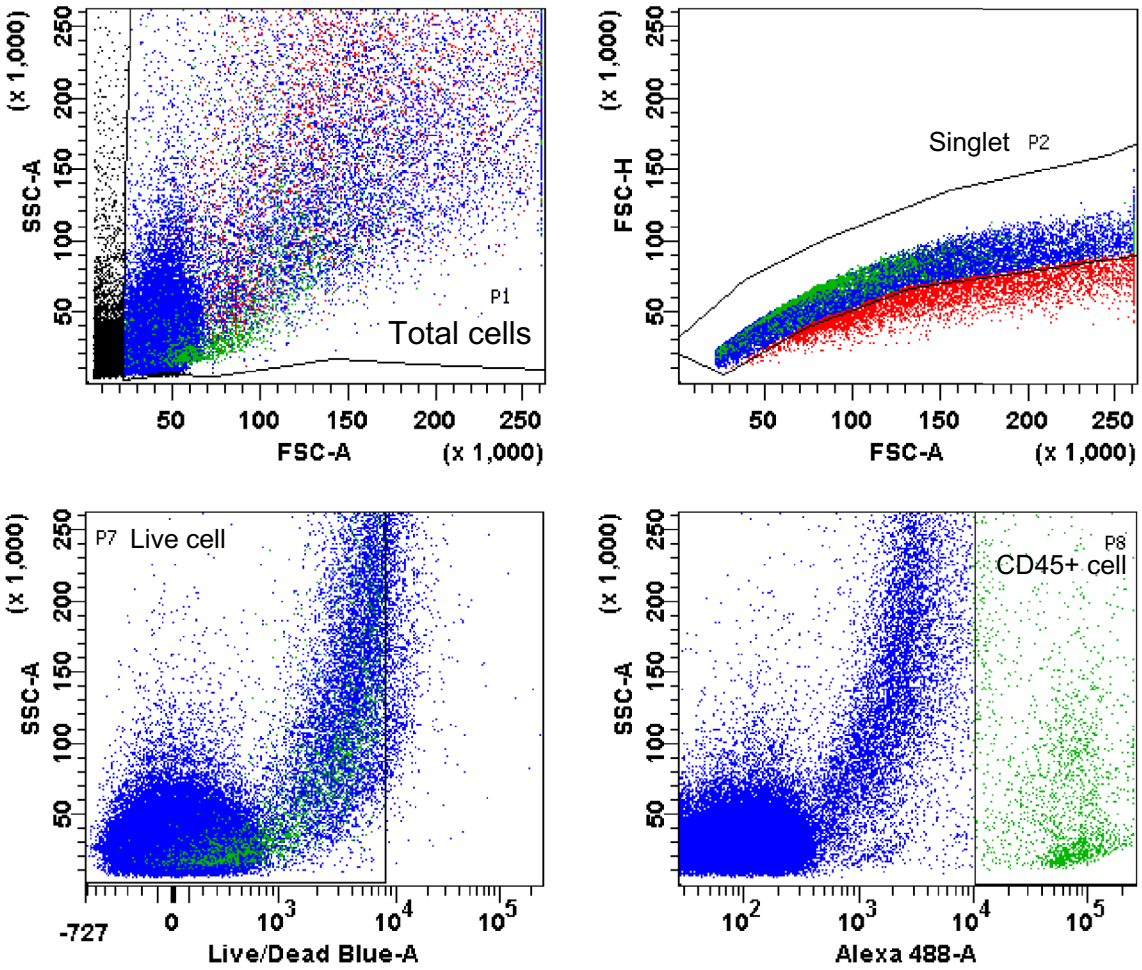

Supplementary Figure 2

a

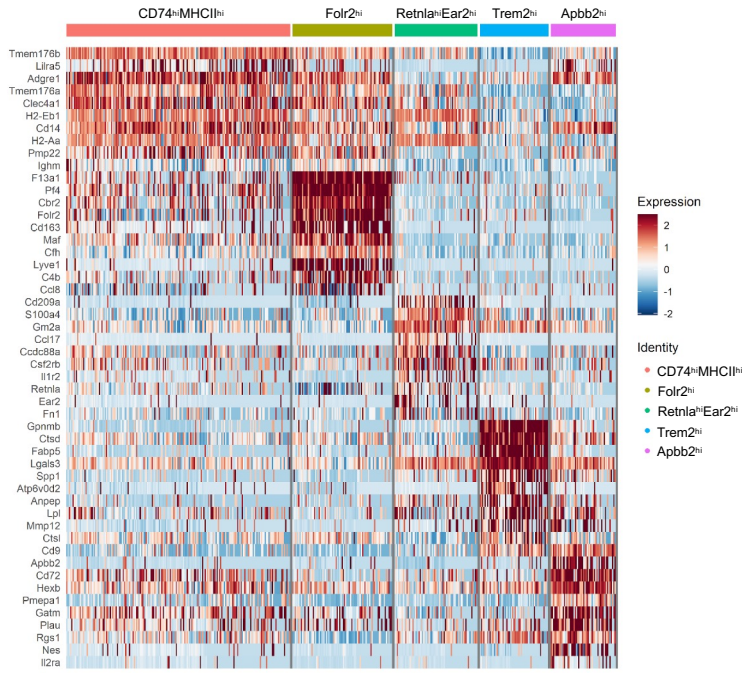

b

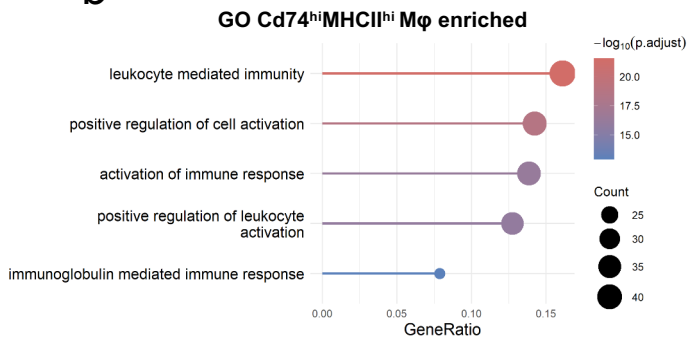

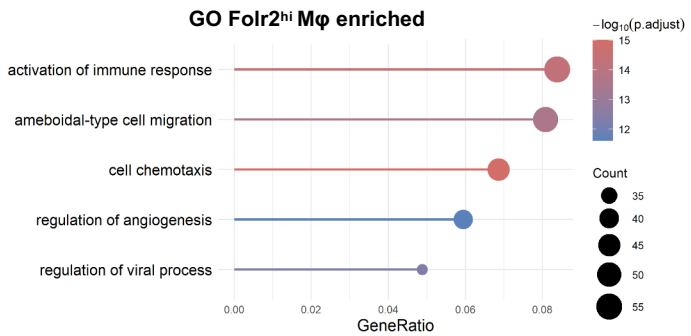

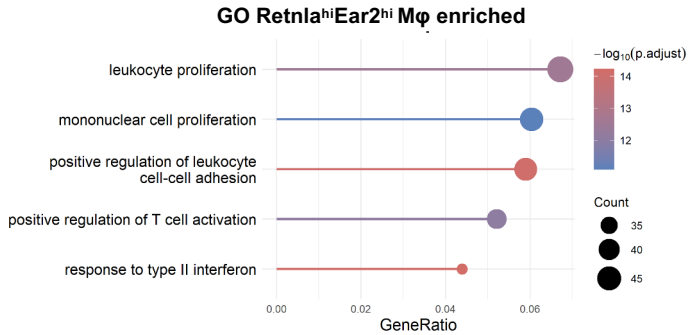

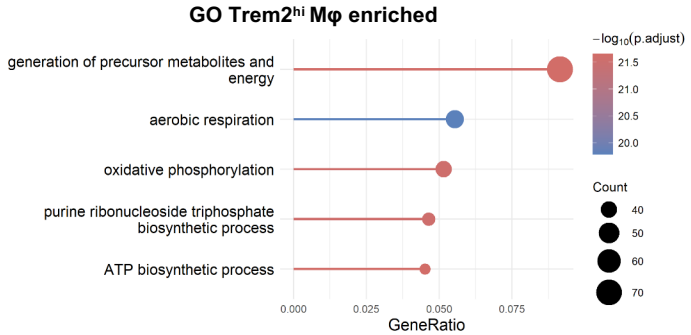

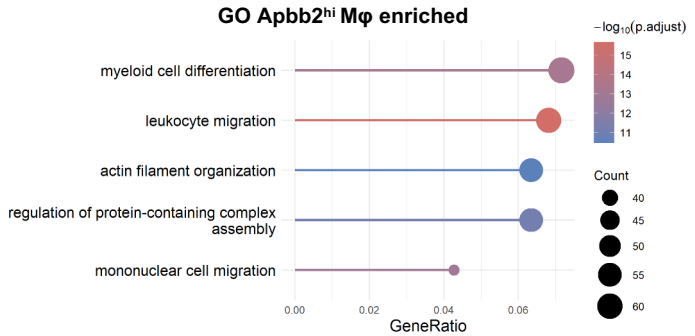

Supplementary Figure 3

a

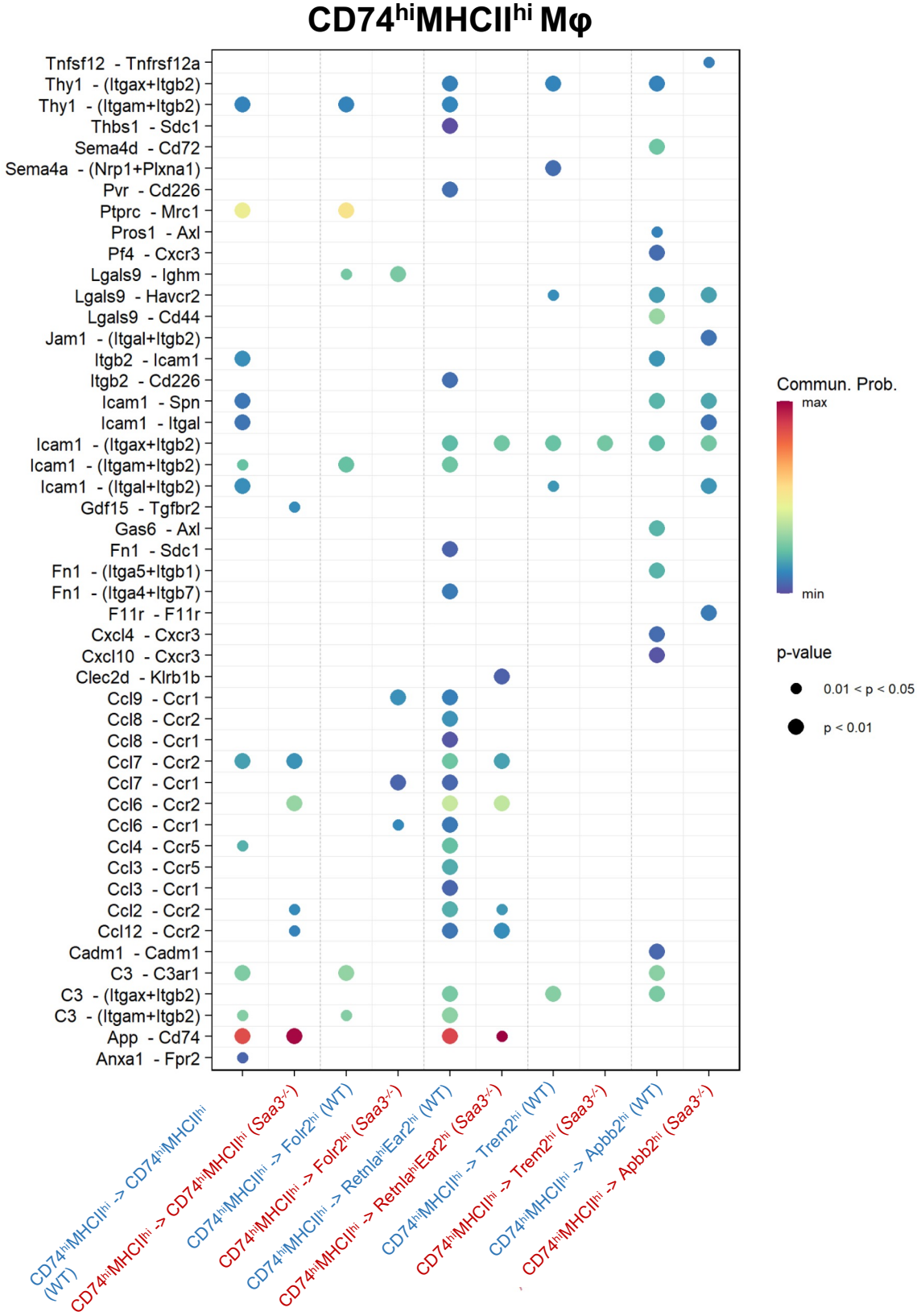

Supplementary Figure 3

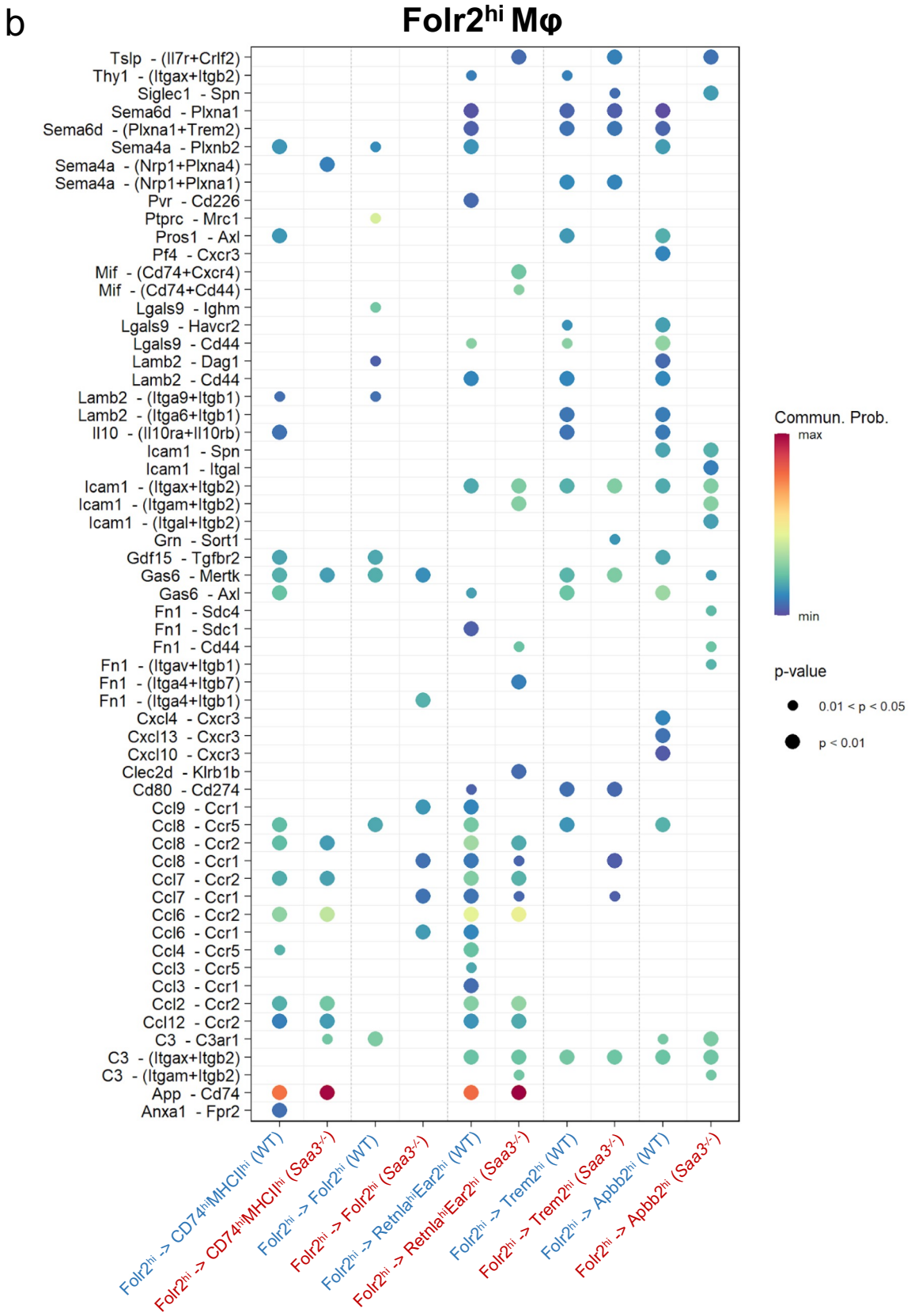

Supplementary Figure 3

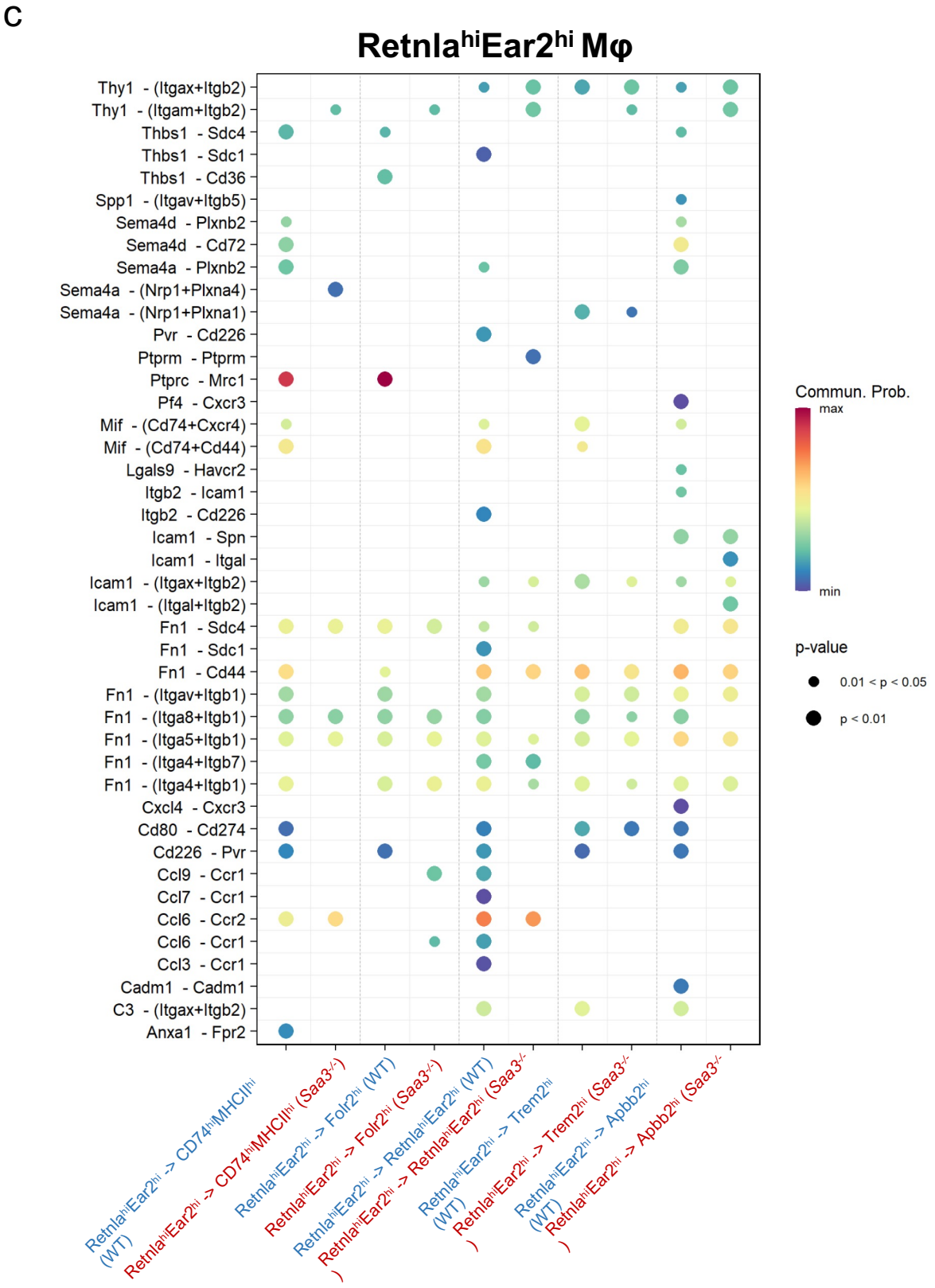

Supplementary Figure 3

d

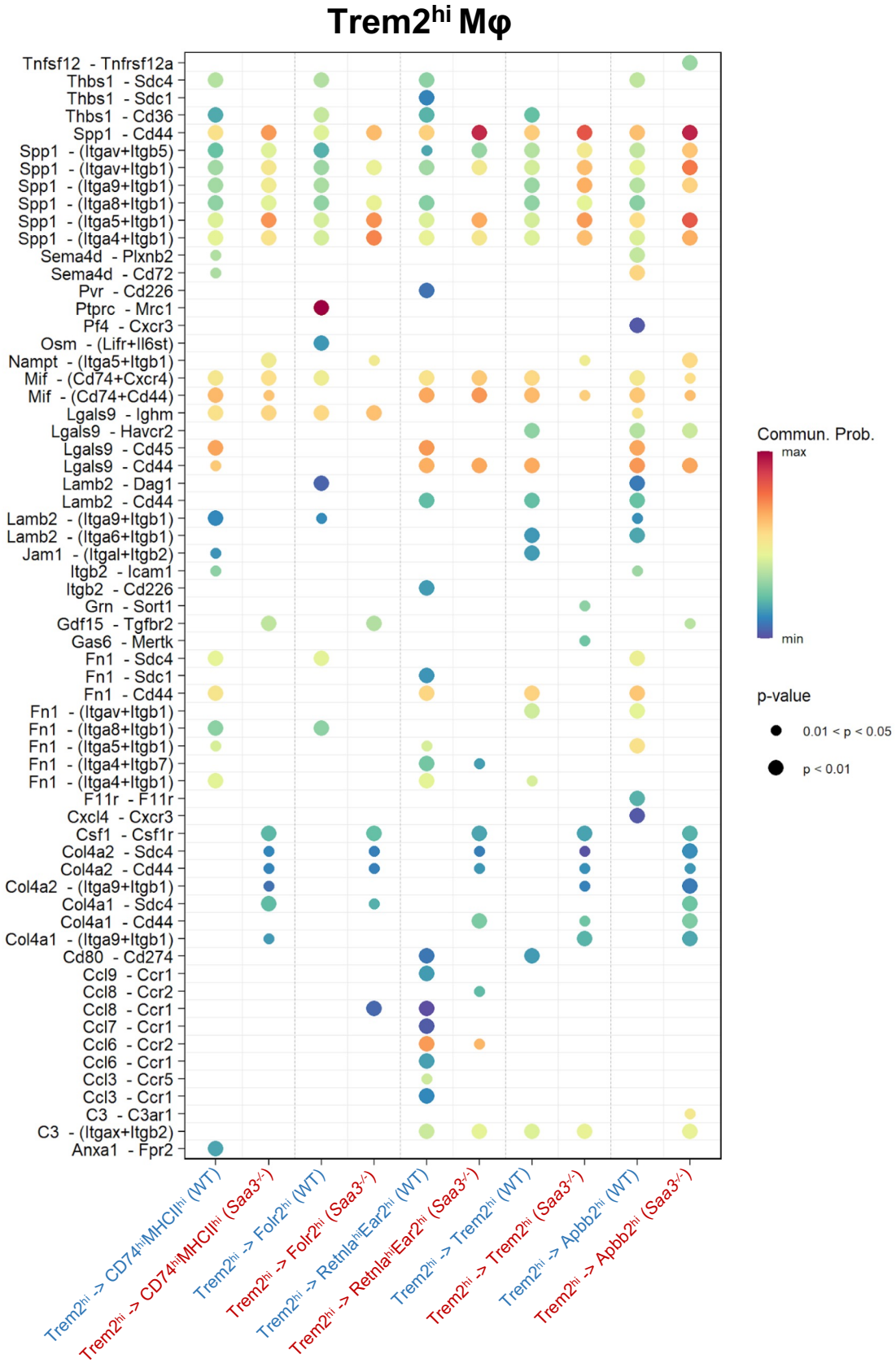

Supplementary Figure 3

e

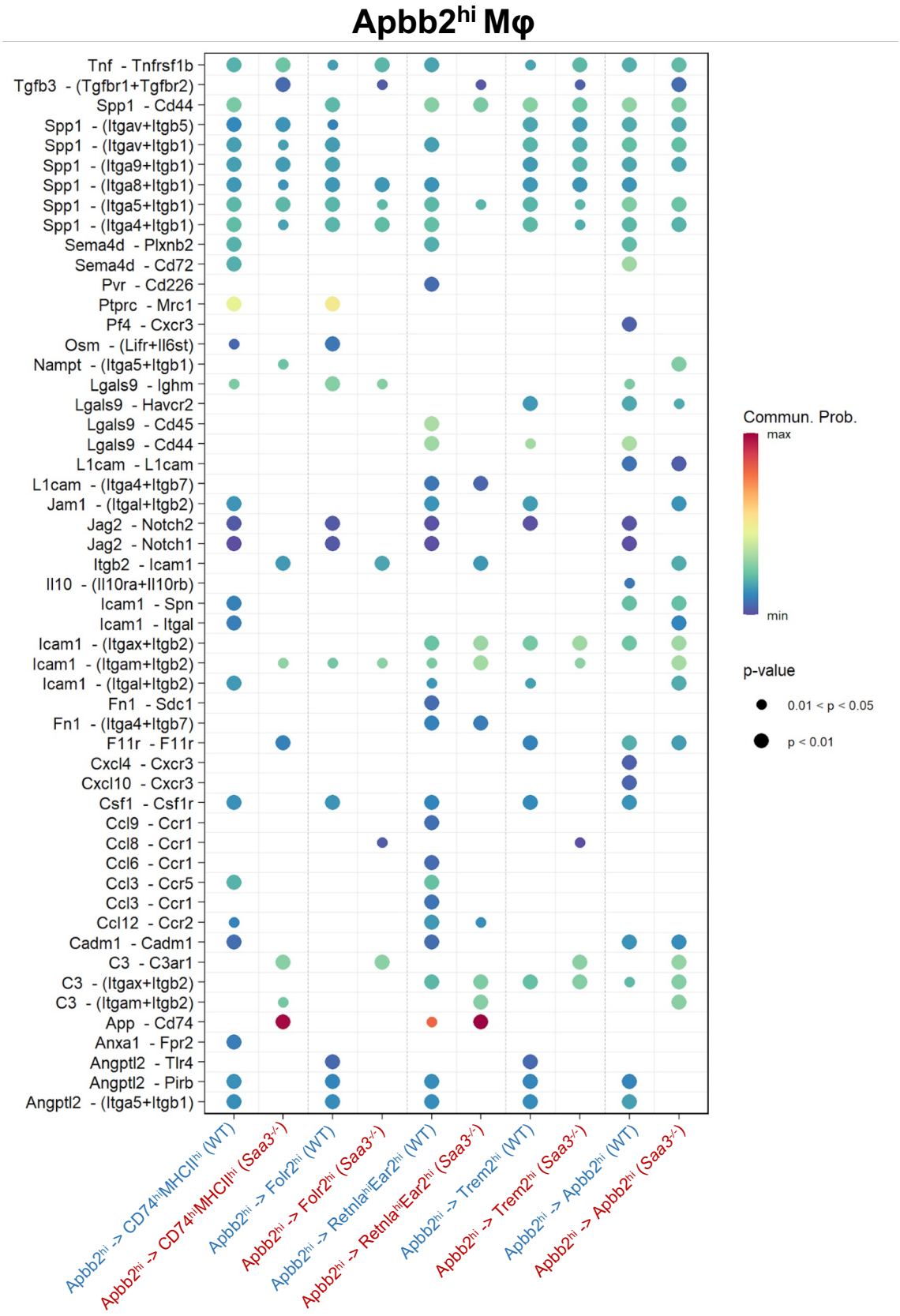
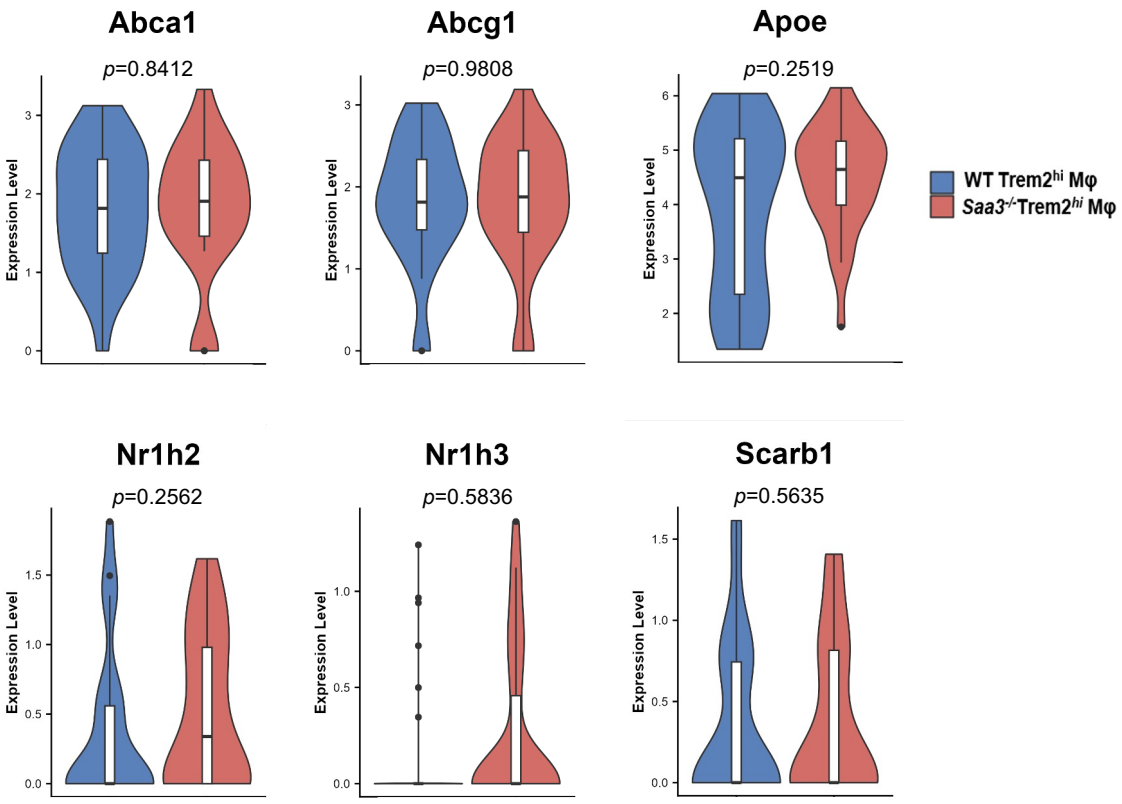
Supplementary Figure 4